JAMES Journal of Advances in Modeling Earth Systems

RESEARCH ARTICLE
10.1029/2026MS005781

Characteristics of a Multi-Model Ensemble of Mock-Walker Simulations

Graham L. O'Donnell[1], Allison A. Wing[1], Levi G. Silvers[2], Kevin A. Reed[3], Peter A. Bogenschutz[4], Jean-Pierre Chaboureau[5], Guy Dagan[6], Romain Fiévet[7], Blaž Gasparini[8], Walter M. Hannah[4], Keiichi Hashimoto[9,10], Peter G. Hill[11,12], Gabrielle "Bee" R. Leung[2,13], Shuhei Matsugishi[14], Sebastian Ortega[7], Romain Roehrig[15], David M. Romps[16,17], Jacob Shpund[6,18], Adam B. Sokol[19], Lorenzo Tomassini[20,21], Susan C. van den Heever[2], and Chien-Ming Wu[22]

[1]Department of Earth, Ocean and Atmospheric Science, Florida State University, Tallahassee, FL, USA, [2]Department of Atmospheric Science, Colorado State University, Fort Collins, CO, USA, [3]School of Marine and Atmospheric Sciences, Stony Brook University, Stony Brook, NY, USA, [4]Lawrence Livermore National Laboratory, Livermore, CA, USA, [5]LAERO, Université de Toulouse, CNRS, IRD, Toulouse, France, [6]Institute of Earth Sciences, Hebrew University of Jerusalem, Jerusalem, Israel, [7]Max Planck Institute for Meteorology, Hamburg, Germany, [8]Department of Meteorology and Geophysics, University of Vienna, Vienna, Austria, [9]Department of Earth and Planetary Science, The University of Tokyo, Tokyo, Japan, [10]Research Center for Environmental Modeling and Application, Japan Agency for Marine-Earth Science and Technology, Yokohama, Japan, [11]Department of Meteorology, University of Reading, Reading, UK, [12]Now at European Centre for Medium-Range Weather Forecasts, Reading, UK, [13]Department of Atmospheric and Oceanic Sciences, University of Wisconsin–Madison, Madison, WI, USA, [14]Atmosphere and Ocean Research Institute, The University of Tokyo, Kashiwa, Japan, [15]Météo France, CNRS, Université de Toulouse, CNRM, Toulouse, France, [16]Department of Earth and Planetary Science, University of California, Berkeley, CA, USA, [17]Climate and Ecosystem Sciences Division, Lawrence Berkeley National Laboratory, Berkeley, CA, USA, [18]Israel Meteorological Service, Beit Dagan, Israel, [19]Program for Atmospheric and Oceanic Sciences, Princeton University, Princeton, NJ, USA, [20]Met Office, Exeter, UK, [21]School of Mathematics, University of Leeds, Leeds, UK, [22]Department of Atmospheric Sciences, National Taiwan University, Taipei, Taiwan

Key Points:

- Even with a forced mock-Walker circulation, a wide variety of convective structures form across idealized model simulations
- Given mean surface warming, climate sensitivity decreases with increasing sea surface temperature gradient
- The degree of aggregation increases in response to a forced overturning circulation

Supporting Information:

Supporting Information may be found in the online version of this article.

Correspondence to:

G. L. O'Donnell,
glodonnell@fsu.edu

Citation:

O'Donnell, G. L., Wing, A. A., Silvers, L. G., Reed, K. A., Bogenschutz, P. A., Chaboureau, J.-P., et al. (2026). Characteristics of a multi-model ensemble of mock-Walker simulations. *Journal of Advances in Modeling Earth Systems*, *18*, e2026MS005781. https://doi.org/10.1029/2026MS005781

Received 26 JAN 2026
Accepted 12 JUL 2026

Abstract

The Radiative-Convective Equilibrium Model Intercomparison Project (RCEMIP) phase I provided insights into the tropical radiative-convective equilibrium state across an unprecedented ensemble of models that includes both those with parameterized and explicit convection. RCEMIP phase II (RCEMIP-II) introduces mock-Walker simulations to examine how sea surface temperature (SST) gradients and the forced circulation they theoretically induce interact with the structure of convection and mean climate state. This overview paper presents descriptions of and initial results from 17 numerical models regarding clouds, convective organization, and circulation structure. Results regarding warming the mean SST in the presence of an SST gradient generally mirror those from RCEMIP-I but a larger range of dynamical circulations, along with additional phenomena, are possible in RCEMIP-II. Increases in the SST gradient while the mean SST is held constant lead to more convective organization across many models, as measured by a number of organization metrics. Increases in the SST gradient also tend to decrease the frequency of high, thin clouds while increasing the frequency of low clouds, including the possibility of stratocumulus, which were not seen in RCEMIP-I. RCEMIP-II also provides an estimate of the influence of a pattern effect, suggesting increased negative climate feedbacks if increases in the SST gradient occur alongside mean warming. However, the SST gradient's inability to fully constrain the circulation structure allows simulations to show varying importance of self-aggregation and forced clustering over the warm pool, resulting in extreme variety in the circulation structures and important climate variables in the organized state across the model ensemble.

Plain Language Summary

A previous research project used a simplified model configuration to examine the behavior of clouds and cloud clusters in the tropical climate, as well as their implications for climate science, across a large number of computer simulations. This study moves one step closer to reality by including the existence of warmer and cooler regions of the tropical oceans while still including many models. These models produce a wide variety of simulated climates, but by comparing them we can find robust results. If we increase the temperature difference between the warm and cool oceans, storms tend to cluster more over the warmest water instead of forming clusters on their own everywhere. If this occurs alongside global warming, it could help stabilize the climate. Overall, the study can be viewed as a starting point for much more future research.

1. Introduction

The use of model intercomparisons has a long history in climate science. The use of an ensemble of semi-independent models, each with their own configurations and parameters, can help identify results which are independent of implementation rather than dependent on uncertain aspects of a given model (e.g., Gates, 1992). The Radiative-Convective Equilibrium Model Intercomparison Project (RCEMIP; Wing et al., 2018, 2020a) set out to apply this philosophy to the state of tropical radiative-convective equilibrium (RCE), the simplest framework for understanding many important features of the tropical climate (Manabe & Strickler, 1964). Three scientific questions were key foci for RCEMIP (Wing et al., 2018):

- What is the response of clouds to warming and the climate sensitivity in RCE?
- What is the dependence of convective aggregation and tropical circulation regimes on temperature in RCE?
- What is the robustness of the RCE state, including the above results, across the spectrum of models?

Data from approximately 30 models were submitted for the RCEMIP-I data set, including a wide variety of model types: cloud-resolving models (CRMs), general circulation models (GCMs), single-column models (SCMs), large eddy simulations (LESs), and global cloud-resolving models (GCRMs) all participated. Many results have been derived from RCEMIP and other studies inspired by the RCEMIP configuration regarding external forcing (Dagan et al., 2025), convective organization, the tropical climate, and key interactions between the two. Physical processes driving convective organization have been a key focus, with many studies continuing to demonstrate that the feedback between longwave radiation and clouds is critical (Coppin & Roehrig, 2022; Pope et al., 2021, 2023), though other factors like surface fluxes (Coppin & Roehrig, 2022) and shallow circulations (Pope et al., 2021) also play a role. The result of these feedbacks is an exceptional variety of organized states and no consensus on the response of organization to warming. With or without the presence of aggregation, the ensemble shows huge spreads in modeled profiles of temperature, humidity, stability, and other factors (Silvers et al., 2023; Sokol & Hartmann, 2022; Wing & Singh, 2024; Wing et al., 2020a). The response of the large-scale circulations to warming in the presence of aggregation has also been studied, with the increased stability in the free troposphere of the dry regions slowing subsidence, decreasing ascent fraction and slowing the circulation overall (Jenney et al., 2020; Silvers et al., 2023). Cloud responses to warming are also a prominent topic of investigation, with studies focusing on the increase in height and decrease in area of thick anvil clouds (Reed et al., 2021; Sokol et al., 2024; Stauffer & Wing, 2022). Ultimately, the above changes to high clouds among other factors link convective organization to climate sensitivity (Becker & Wing, 2020; Bourdin et al., 2021; Mackie & Byrne, 2023; Stauffer & Wing, 2023, 2024). While many of these patterns were seen in earlier work, the fact that the conclusions hold across the RCEMIP ensemble demonstrates their robustness.

RCEMIP phase II (RCEMIP-II) looks to build on RCEMIP-I by moving one step up the model hierarchy (Held, 2005; Jeevanjee et al., 2017) by introducing an SST gradient to implement a mock-Walker configuration (Raymond, 1994). The sinusoidal SST pattern used in RCEMIP-II satisfies the four design principles set forth by Wing et al. (2024) for extending RCEMIP:

1. The ability to directly compare limited-area models with explicit convection and global climate models with parameterized convection
2. Ease of implementation, to encourage the broadest possible participation
3. A continued investigation of the above three themes of RCEMIP while moving a step up the model hierarchy of complexity
4. The provision of an external constraint on convection

Any model capable of running RCEMIP-I's large-domain configuration (`RCE_large`) should be capable of running RCEMIP-II simulations with minimal modification, satisfying principles 1 and 2, although the large domain excludes SCMs (due to their inability to simulate SST gradients) and LESs (as such simulations are only now becoming feasible (e.g., Bogenschutz et al., 2025), with none submitted for RCEMIP-II). The SST gradient moves one step up the model hierarchy toward reality by mimicking the global-scale SST differences driving atmospheric circulations (Back & Bretherton, 2009a; Bretherton & Sobel, 2002; Lindzen & Nigam, 1987). For example, differences between low- and high-gradient simulations are reminiscent of differences in the Walker circulation between El Niño and La Niña. More generally, varying combinations of the gradient and mean values of SST allows for examination of climate features like stratocumulus and its transition to deep convection, or the pattern effect (Andrews et al., 2022; Fueglistaler & Silvers, 2021). Though simplified, mock-Walker simulations capture many important features of both the tropical circulations in general (Blossey et al., 2010; Grabowski et al., 2000; K. Larson & Hartmann, 2003) and the specific regions where deep convection occurs (Bretherton et al., 2006). The simulations are well suited for furthering the study of self-aggregation: no simpler setup can examine the mutual interaction of convective self-aggregation with the forced overturning circulation. Importantly, the modeled convection in mock-Walker simulations often occurs in a smaller region than would be expected directly from the SST pattern itself, in part due to self-aggregation-like effects (Bretherton & Sobel, 2002; Grabowski et al., 2000; Liu & Moncrieff, 2008). Overall, prior mock-Walker simulations exhibit a rich array of processes relating circulation and convection (Dagan et al., 2023; Kuang, 2012; Liu & Moncrieff, 2008; Lutsko & Cronin, 2024; Sokol et al., 2025; Stephens et al., 2008; Tompkins, 2001; Wofsy & Kuang, 2012), and the intercomparison provided by RCEMIP-II allows analysis of the robustness of these processes and features of the interaction of self-aggregation and circulation.

As Wing et al. (2020a) accomplished for RCEMIP-I, the goals of this overview paper include documenting the RCEMIP-II data set, highlighting key features, and presenting early scientific results. This is intended to provide a basic comparison with RCEMIP-I and establish some frameworks which may be useful for future RCEMIP research. Section 2 describes the simulation setup in more depth, focusing on the key differences from RCEMIP-I. Section 3 provides a first qualitative look at the simulations, showing the modeled spatiotemporal structure. Section 4 quantifies the degree and structure of convective organization with both a variety of organization metrics and a novel classification based on the spatial structure of column relative humidity (CRH). Section 5 analyzes some basic features of the climate state, including domain-mean hydrological and radiative variables, the cloud distribution, the connection to the pattern effect, and changes in the hydrological cycle.

2. RCEMIP Phase II

The model configuration for RCEMIP-II is described in Wing et al. (2024), with most parameters carried over from RCEMIP-I as described in Wing et al. (2018). Overall, the RCEMIP-II mock-Walker "`MW`" configuration is identical to that of RCEMIP-I's large-domain (`RCE_large`) configuration except for the addition of an SST gradient. As in RCEMIP-I, each simulation uses a nonrotating aquaplanet with fixed solar radiation and no diurnal cycle. Each simulation is described by a mean SST ($\langle T \rangle$) and a difference between the maximum and minimum SSTs within the domain (ΔT). For example, `MW_300dT1p25` describes the simulation with $\langle T \rangle = 300$ K and $\Delta T = 1.25$ K. Five simulations are run for each model:

1. `MW_295dT1p25`
2. `MW_300dT0p625`
3. `MW_300dT1p25`
4. `MW_300dT2p5`
5. `MW_305dT1p25`.

The RCEMIP ensemble includes both CRMs, run on a long-channel domain (approximately 6,000 × 400 km) at 3-km resolution to explicitly resolve convection, and GCMs, run at around 1-degree resolution on an Earth-sized aquaplanet. At the time of this paper's preparation, 17 models have submitted data: 11 CRMs and 6 GCMs (Table 1).

For CRMs, the SST pattern is given as $\mathrm{SST}(x) = \langle T \rangle - \frac{\Delta T}{2}\cos\left(\frac{2\pi x}{L_x}\right)$, where $L_x \approx 6000$ km is the length of the domain. This creates a "warm pool" in the center of the domain with cooler waters around it. In GCMs, a similar SST gradient is created by using SST as a function of latitude ϕ: $\mathrm{SST}(\phi) = \langle T \rangle - \frac{\Delta T}{2}\cos\left(\frac{2\pi\phi}{\lambda}\right)$. When λ is set to $\frac{3\pi}{10} = 54°$ in an Earth-sized simulation, this creates a wavelength of approximately 6,000 km. If the CRM configuration were rotated 90° and centered on the equator, it would stretch from 27°S to 27°N, span ~4° degrees of longitude, and match the GCM's SST pattern. Note that the equatorial warm band is not the only warm region in the GCM simulations, as there are two other warm bands at latitudes $\pm\lambda$, usually 54°N/S. This pattern does increase the global-mean SST to $\langle T \rangle + 0.011\Delta T$, but this change is likely too small (≈0.01 K) to noticeably affect the resulting climate. These configurations are compared to RCEMIP-I in Figure 1.

In RCEMIP-I, the effect of changes in the mean SST could be studied. In RCEMIP-II, we now have two dimensions of changes in SST to examine: changes in the mean SST while the SST gradient is fixed and changes in the SST gradient while the mean SST is fixed. Pattern changes where the mean SST and SST gradient change

Table 1
The Models Participating in the Radiative-Convective Equilibrium Model Intercomparison Project Phase II (RCEMIP-II)

Model		Model type
• *DAM*	Das Atmosphaerische Modell	CRM
• *ICON-CRM*	ICOsahedral Nonhydrostatic model—Sapphire	CRM
• *MESONH*	MESO-NH v5.6	CRM
• RAMS	Regional Atmospheric Modeling System version 6.3.04	CRM
• *SAM-CRM*	System for Atmospheric Modeling, single-moment microphysics	CRM
• SAM-M2005	System for Atmospheric Modeling, M2005 microphysics	CRM
• SAM-P3ice	System for Atmospheric Modeling, P3ice microphysics	CRM
• *SCALE*	Scalable Computing for Advanced Library and Environment v5.2.5	CRM
• SCREAMv0	Simple Cloud Resolving E3SM Atmosphere Model	CRM
• *UKMO-RA1-T*	UK Met Office idealized model v11.0	CRM
• VVM	Vector Vorticity Model	CRM
× *CAM6*	Community Atmosphere Model version 6	GCM
× *CNRM-CM6*	CNRM-CM6-1—atmosphere component	GCM
× E3SMv3	Energy Exascale Earth System Model	GCM
× E3SM-MMFv2	Super-parameterized Energy Exascale Earth System Model	GCM
× MIROC6	Model for Interdisciplinary Research on Climate	GCM
× *UKMO-GA7.1*	Met Office Unified Model Global Atmosphere v7.1	GCM

Note. The symbols show the colors used for each model in subsequent plots. When both CRMs and GCMs are included in a plot, each CRM is represented by a circle while each GCM is represented by a cross. Models in italics also participated in RCEMIP-I.

simultaneously can be seen as varying in both dimensions at once. Examining the simulations across changes in $\langle T \rangle$ is broadly comparable to the analyses performed in RCEMIP-I, though the presence of distinct warm and cool regions could cause unexpected differences in behavior from the previous work. Examination of changes in ΔT has no analogue in RCEMIP-I.

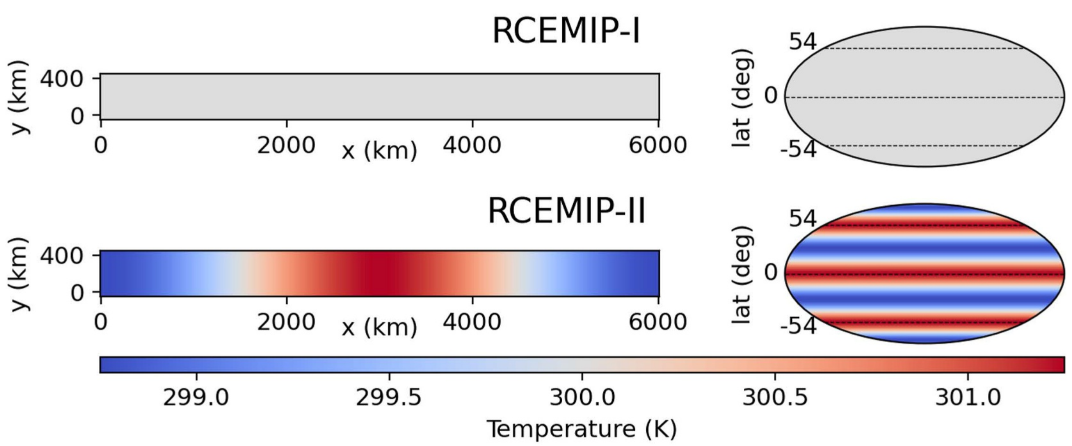

Figure 1. Sea surface temperature (SST) patterns of each Radiative-Convective Equilibrium Model Intercomparison Project (RCEMIP) configuration. The top row depicts RCEMIP-I's large-domain configuration with a constant SST. The bottom row shows RCEMIP-II's `300dT2p5` SST pattern, with a central warm pool in the cloud-resolving model configuration (left) and several warm bands in the general circulation model (GCM) configuration (right). A Mollweide projection is used for GCM plots in this paper, as in Wing et al. (2020a).

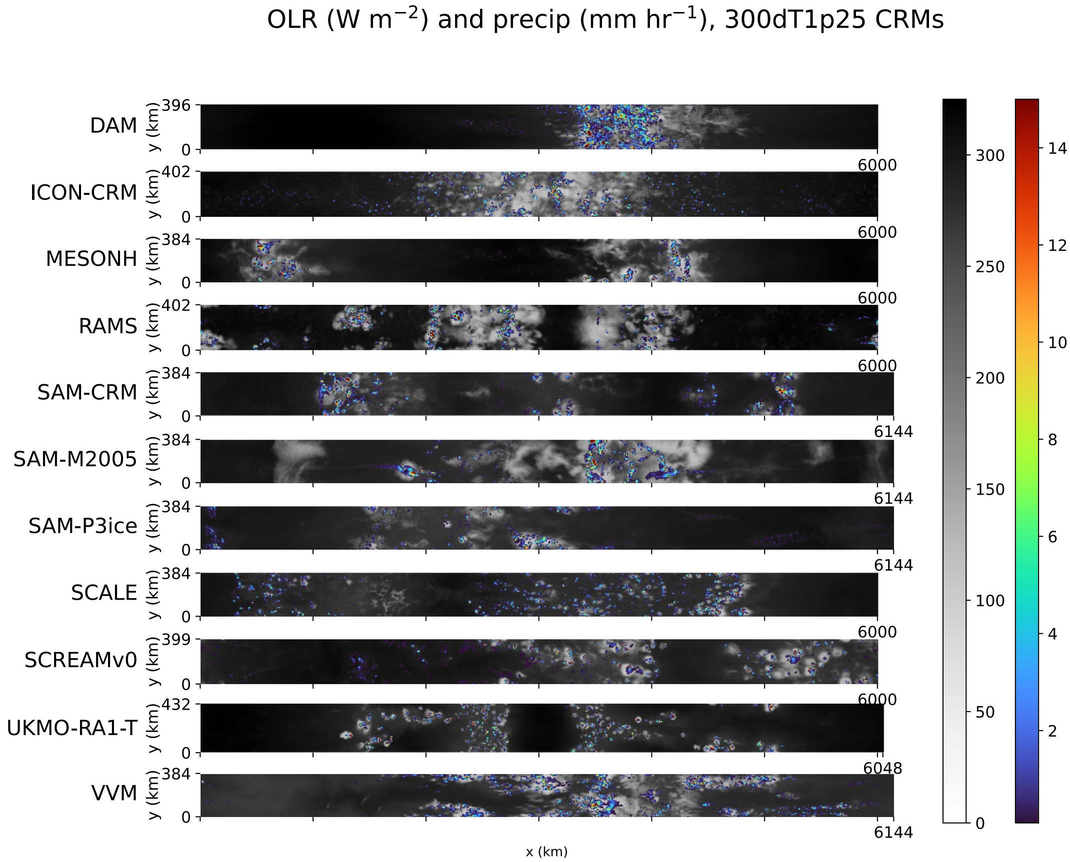

Figure 2. Snapshots of outgoing longwave radiation (W m^{-2}; grayscale) and surface precipitation (mm h^{-1}; colors) for each CRM's `300dT1p25` simulation 10 days before the end. Tick-marks on the *x*-axis are shown every 1,000 km.

3. Spatiotemporal Structure of Simulations

3.1. Spatial Structure

Convective organization manifests via the formation of large-scale moist and dry regions spanning hundreds or thousands of kilometers. In the long-channel CRM domain, these moist regions often form as several bands of convection spanning the narrow dimension of the domain. Figure 2 shows a snapshot of each CRM taken 10 days before the end of the `300dT1p25` simulation, 190 days after initialization. All 11 CRMs show the banded pattern to some degree, exhibiting between one (DAM, SAM-P3ice) and four (SAM-CRM) bands of convection at the instant chosen. They mostly favor convection over the central warm pool and often have a large clear region over the cold portion of the domain, but several models still have convective cells or bands in the cooler areas.

In the GCMs, convection is able to aggregate in both dimensions. Meridionally, this can be guided by the SST pattern's three warm bands, while zonally these simulations can only form clusters via self-aggregation. These structures can be seen in Figure 3, also 10 days before the end of the simulations. The structure shared by most models is a broken band of convection along the equator with some dry regions mixed in, along with moist clusters over the high-latitude warm bands. Other than the preference for convection over warmer SSTs, these structures in both CRMs and GCMs are reminiscent of those in RCEMIP-I as seen in Figures 4 and 5 of Wing et al. (2020a).

Time-averaged versions of these figures for the CRMs and GCMs are included as Figures S1 and S2 in Supporting Information S1, respectively. The CRMs still show a variety of structures, with some models showing a sharp peak in precipitation over the center of the warm pool, some still showing two or three distinct bands of precipitation, and some showing some amount of precipitation smeared across the whole domain. Most of the GCMs show three zonally-symmetric bands corresponding to the three warm bands and showing that their convection

10.1029/2026MS005781

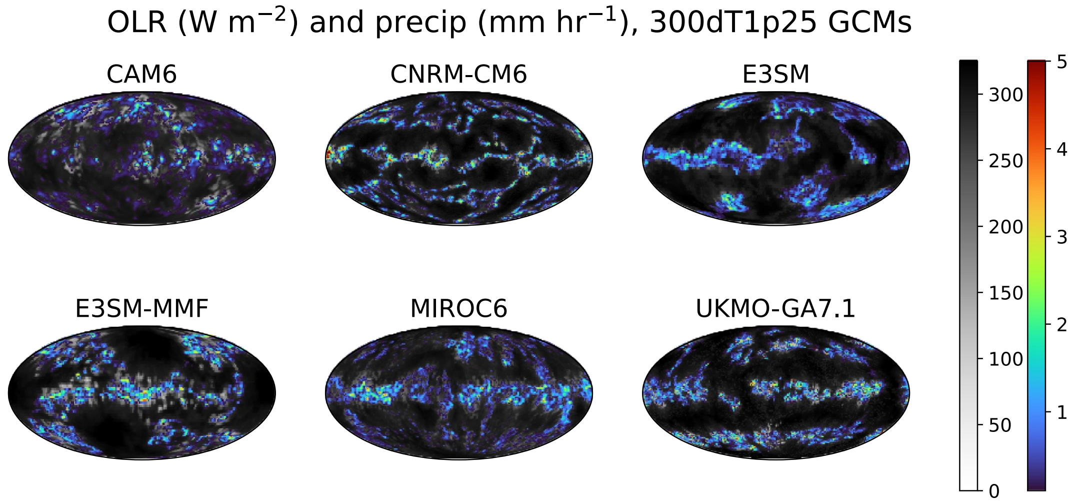

Figure 3. Snapshots of outgoing longwave radiation (W m^{-2}; grayscale) and surface precipitation (mm h^{-1}; colors) for each GCM's `300dT1p25` simulation 10 days before the end. The scale for precipitation is different than in Figure 2.

shifts in longitude over time, though one model (E3SM-MMF) still shows zonal asymmetry: even over 1,000 days, its convective regions remain fixed in place.

In addition to this examination of the horizontal structure of the simulations, we examined the vertical structure of the overturning circulations. Time-averaged plots of streamfunction and relative humidity for the CRM simulations with $\langle T \rangle = 300$ K are given as Figure 4, focusing on the effect of changing the SST gradient. Figure S3 in Supporting Information S1 shows a similar plot for the simulations with $\Delta T = 1.25$ K. Consistent with prior mock-Walker studies (e.g., Grabowski et al., 2000; Lutsko & Cronin, 2024; Yano et al., 2002), many of the simulations display multiple vertically-stacked cells, with the majority of the simulations showing either two or three such cells. The overturning circulations depicted in these streamfunction plots are usually stronger and better defined in the time-average (and thus most consistently present) for the higher-gradient `300dT2p5` simulations. However, even in the `300dT0p625` simulations a large-scale forced overturning circulation can be seen in some models when the time average is taken with rising motion seen over the warmest SSTs, bounded by a large counterclockwise cell to the left and a large clockwise cell to the right. As also seen in Figure S1 in Supporting Information S1, many of the CRMs have moist regions that stay in one place for the full duration of the time average, and these distinct regions can be seen in Figure 4. A more detailed analysis of these circulation structures in 3D should be considered for future work.

3.2. Temporal Variability

The temporal evolution of organized structures in the `300dT1p25` simulations is seen in Hovmoller diagrams of CRH in Figure 5. Figures S4–S7 in Supporting Information S1 show these diagrams for the other four simulations. For the CRMs in the top row, CRH is averaged over the entire length of the short y-dimension. For the GCMs in the bottom row, a slice 4° of longitude wide is chosen such that the cumulative distribution function (CDF) of CRH within that slice is most similar to the CDF of CRH for the full tropical band. This creates a representative slice for each GCM in the same shape as the CRM domain for a fair comparison. Note that as GCM convection aggregates in both dimensions, it is possible for this slice to fall in between moist regions and thus intersect only dry regions at times, which is seen in most of the models shown. In Figure 5, the slices for all GCMs do intersect moist regions: E3SM, E3SM-MMF, and MIROC6 simply have particularly narrow CRH distributions, so appear drier than other models. Both model classes are limited to showing only the first 200 days, which is the full length of the CRM simulations. This allows a visual comparison of the formation of organization across model classes at the same timescales despite the GCM simulations' much longer simulation time. As CRH in the tropics is closely associated with vertical motion, these plots also depict the structure of large-scale overturning circulations.

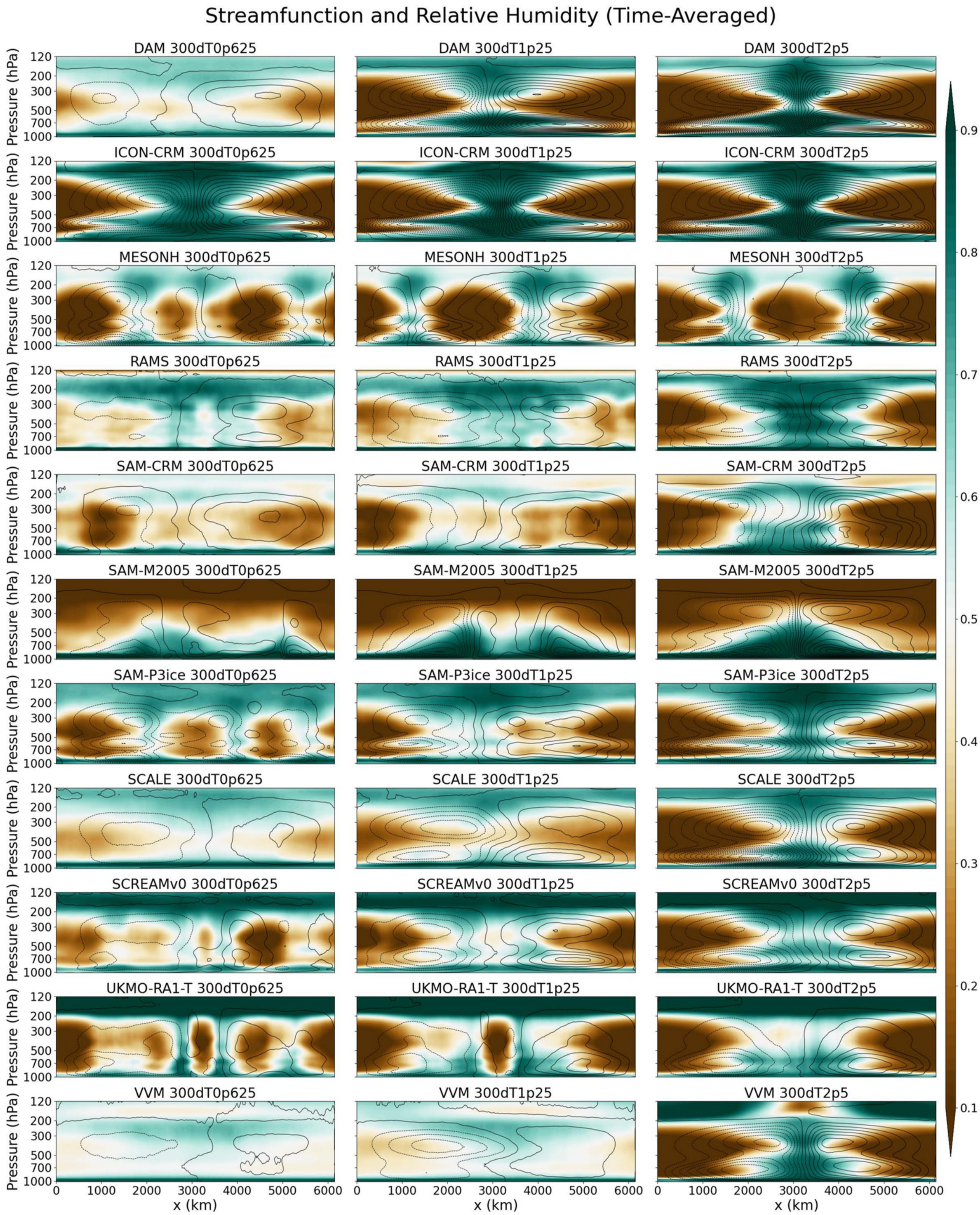

Figure 4. Streamfunction (contours) and relative humidity (shaded) for each cloud-resolving model simulation with a mean sea surface temperature of 300 K, averaged over the final 100 days of each simulation. Relative humidity is calculated relative to liquid above freezing and ice below freezing.

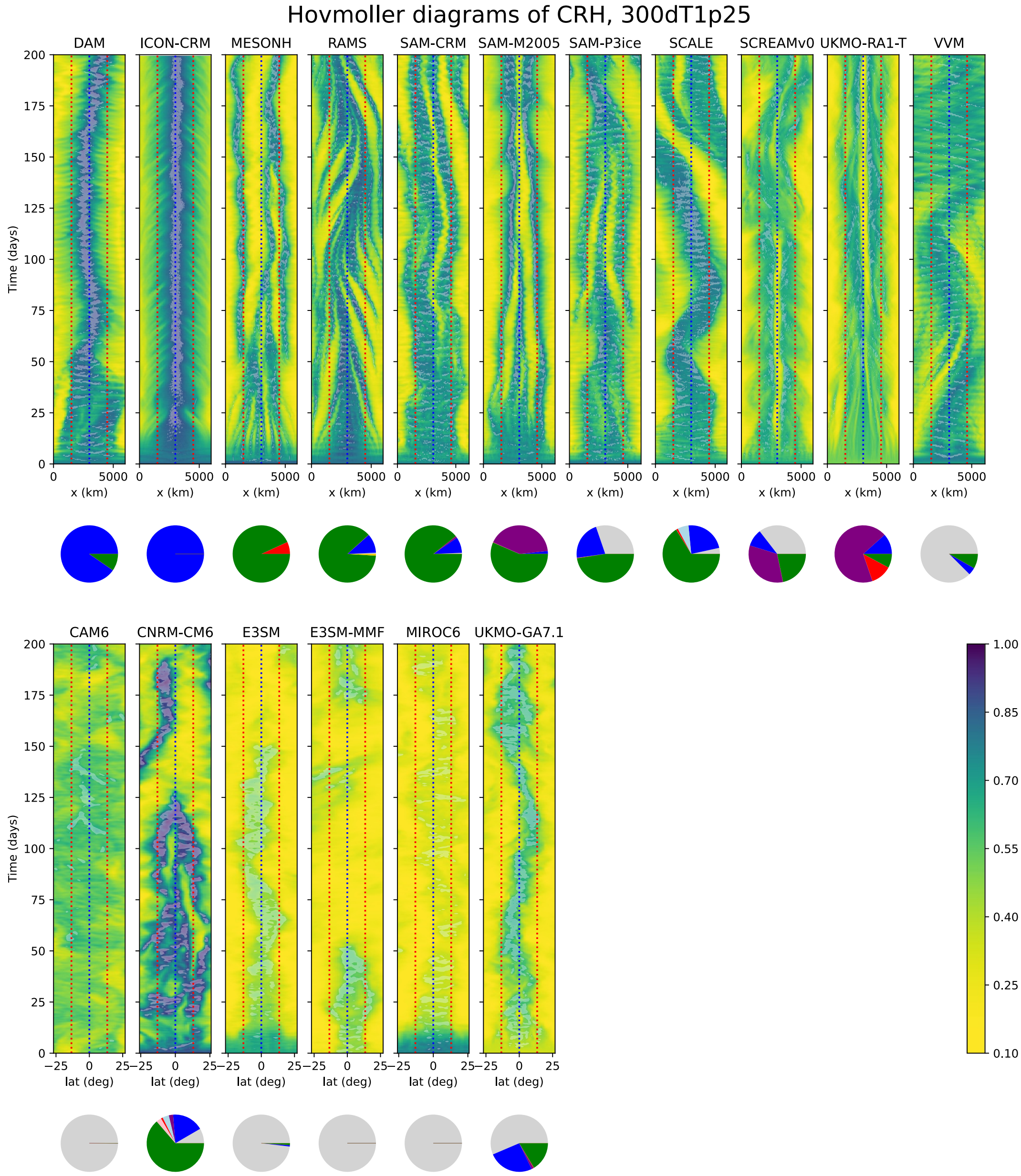

Figure 5. Hovmoller diagrams presenting column relative humidity of the `300dT1p25` simulation for each model. Cloud-resolving models (CRMs) (top row) show the full domain, while general circulation models (GCMs) (bottom row) show a representative slice 4° of longitude wide between 27°S and 27°N. Both CRMs and GCMs are averaged over the shorter dimension of this rectangular domain. Each plot shows the first 200 days of the simulation. White shading indicates locations where precipitation exceeds 0.5 mm/hr. The blue dotted line shows the location of the maximum sea surface temperature (SST) while the red dotted lines mark the location of the maximum SST gradient. The pie charts show the frequency of each Fourier classification, described in Appendix B, after day 75 of each simulation. In the pie charts, blue denotes "peak" classification, red denotes "flank" classification, green denotes "self" classification, purple denotes "splitpeak" classification, and gray denotes "disorganized" classification.

In most models, the first few days show a CRH pattern similar to the SST distribution, with a moister ascending region developing in the warmer center. Over the next several months, some form of organized structure tends to develop. While these organized states are representative of the simulations, they are not necessarily steady states, as there are often still major structural changes involving mergers or splits of moist bands. In one case (VVM), there is even a complete disorganization in the final 75 days as the model spontaneously develops a domain-mean wind shear of ~10 m/s, reminiscent of the QBO-like structures seen by Held et al. (1993) in similar simulations.

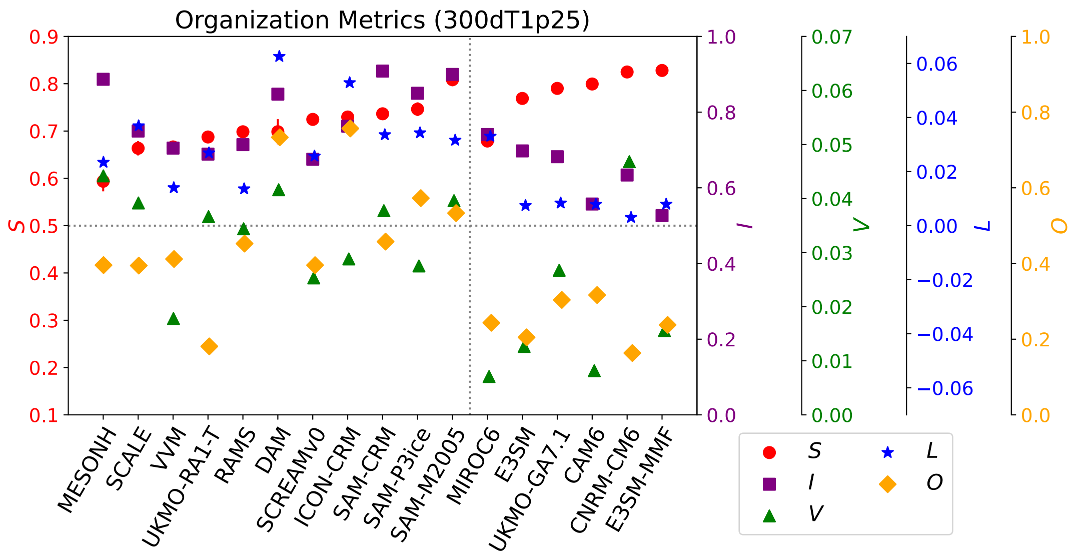

Figure 6. Values of each organization metric for the `300dT1p25` simulations. Five metrics are shown for all models: subsidence fraction (S), organization index (I), variance of column relative humidity (V), L_{org} (L), and OIDRA (O). The dotted vertical line separates the cloud-resolving models on the left from the general circulation models. For I, L, and S, the dotted horizontal line marks the value above which convection is described as "organized." 2σ error bars have been plotted for each metric as a vertical line segment through the scatter point, but these are only visible for S.

There is frequently long-period time variability, such as the expansion and contraction of the central moist regions at a ~30-day period in SCREAMv0, a behavior which is more common in the `300dT2p5` CRM simulations (Figure S7 in Supporting Information S1). Most CRMs also show short-period (~3–4 day) oscillations in CRH and precipitation, which are reminiscent of how the "quasi-two day oscillations" seen by Grabowski et al. (2000) would act in this larger domain, seemingly related to gravity wave dynamics. Overall, the organized structures are strikingly different across models, and will be described further in Section 4.2.

The rainfall distribution follows a similar spatial pattern to CRH, with deep convection and notable rainfall (white shading in Figure 5) confined to the regions of high CRH. It is notably confined to neither the highest SSTs nor the strongest SST gradients, as would be predicted by theory in the absence of self-aggregation (Back & Bretherton, 2009b; Bretherton & Sobel, 2002; Lindzen & Nigam, 1987). This suggests that even in the presence of a forced overturning circulation, self-aggregation must be accurately modeled to predict convective behavior in these simulations where most of the domain is relatively favorable for convection.

4. Convective Organization

4.1. Degree of Convective Organization

We use five metrics to numerically describe the degree of organization: the three chosen for Wing et al. (2020a) as well as two more recently-developed metrics, all of which are described in Appendix A. No individual metric can describe everything about the organization of a scene, and there is no clear standard, justifying use of several metrics. These five span a wide range of length scales, with I mostly examining small scales (~100 km), S and V mostly examining large scales (>1000 km), and L and O seeing some contribution from all scales.

Figure 6 summarizes the values of each metric for each model for the central `300dT1p25` simulation, as in Figure 12 from Wing et al. (2020a). This same figure reproduced for the other SST patterns is given as Figures S8–S11 in Supporting Information S1. Within each class of models, models are sorted by their value of S. Overall, the spread across models is similar in RCEMIP-I and RCEMIP-II. All simulations are classified as "organized" by all metrics which have a numeric delineation between "disorganized" and "organized" (specifically I, L, and S) with the exception of S for MESONH's `305dT1p25` simulation: a simulation which clearly exhibits organization according to I and L. Across the CRMs, the metrics generally show positive correlation coefficients with each other, but these coefficients are often much too small to be significant. For these `300dT1p25` simulations, the only significant positive correlation is between L and O ($r = 0.73$). When the average of the metrics across the five simulations with different SST distributions is taken, an additional correlation between I and V ($r = 0.61$) appears. Correlations are hard to find across metrics for the GCMs, with a negative correlation between L and S in the `295dT1p25` simulation as the only significant correlation seen. Changes in metrics between simulations will be examined in Section 4.3.

4.2. Structure of Convective Organization

We also introduce an alternative method of classifying convective structures, including the spatial scale of organization, based on a Fourier decomposition of the CRH field. This is inspired by the use of V as an organization metric and the knowledge that the sum of the squares of Fourier coefficients equals the variance. The methodology is described in Appendix B, and results in eight distinct classifications of the organized state based on which Fourier mode explains most of the variance.

This methodology gives more information than a classical single-value organization metric. The methodology as described makes a discrete classification, but can be easily modified to a continuous metric of either the absolute amount of CRH variance in each mode or the fraction explained by each mode, as seen in the two right-hand columns of Figure B1. Unlike other metrics, the classification explicitly includes information about the length scale of convective organization, with a "peak" type structure naturally having a larger scale than the other modes due to its wavenumber-1 structure. While other metrics quantify the degree of organization at a given length scale or range of length scales, only the Fourier technique implies different dominant length scales by reporting different classifications. It also has some basis in the literature, as it is related to techniques performed by Beucler and Cronin (2019) in examining length scales of convective organization. The distinct classifications quantitatively suggest cases where different physical processes act as the primary driver of convective organization. "Peak" cases suggest a link to a Lindzen and Nigam (1987)-type overturning circulation, "flank" cases suggest importance of surface flux feedbacks in a region with sharper boundary layer pressure gradients, and "self" cases suggest the organizing processes seen in RCEMIP-I still dominate the organization of convection. We introduce the classification here as it provides a quantitative measure of patterns instead of relying on visual inspection of the 85 simulations, and may serve as a framework for future studies by our group and others, including a paper in progress that studies the processes developing and maintaining differences in structure.

The classification is examined for all scenes after day 75 in each CRM. Over nearly 165,000 classifiable scenes across the five SST distributions, the most common classifications are "peak," making up 37.6% of scenes, and "self," including another 33.5%. "Disorganized" (19.3%) is also a sizable contributor. "Splitpeak" (5.3%) and "flank" (3.9%) make up most of the remainder, with other types appearing in just one or two simulations each. Changes in these distributions with SST will be explored in Section 4.3.

The frequency of each Fourier classification for each simulation is given as the pie charts below the CRH Hovmoller diagrams in Figure 5 and Figures S4–S7 in Supporting Information S1. In the `MW_300dT1p25` simulations in Figure 5, DAM and ICON-CRM are clearly dominated by a single cluster on the maximum SST and receive the "peak" classification at most times. MESONH, RAMS, SAM-CRM, SAM-M2005, and SAM-P3ice all show multiple clusters for most of the time and receive the "self" classification at most timesteps, with MESONH evolving into the two-cluster "flank" state at the end of the simulation. SCALE is also dominated by the "self" classification: although it only shows one cluster, this cluster moves far off-center and must be maintained by processes other than the effect of the warmest SST. UKMO-RA1-T and the early days of SCREAMv0 are dominated by the two-cluster "splitpeak" state, with a more distinct dry region over the cold SST. VVM is usually disorganized as a domain-mean wind shear spontaneously develops in the simulation. Across the ensemble, the vast majority of CRM scenes where domain-mean wind shear exceeds 2 m/s are classified as "disorganized" (not shown). The spontaneous development of wind shear in an initially symmetric environment as in Held et al. (1993) is undesirable and could be prevented by nudging the domain-mean horizontal wind profile to 0, which could allow more scenes to exhibit organized classifications. The GCMs are most often classified as "disorganized," both because they usually have smaller variability in CRH and because the slice chosen often misses all convection. An updated method would be needed to properly characterize them.

Figure 7 shows an example of how the Fourier classification relates to other metrics, in this case L. While there is a large spread in the values of L seen for scenes exhibiting each classification structure, the "peak" structure shows a much higher average value of L than other structures, and the "disorganized" structure has a low average value of L. Figure S12 in Supporting Information S1 shows a similar plot using I. Though it shows less variation between

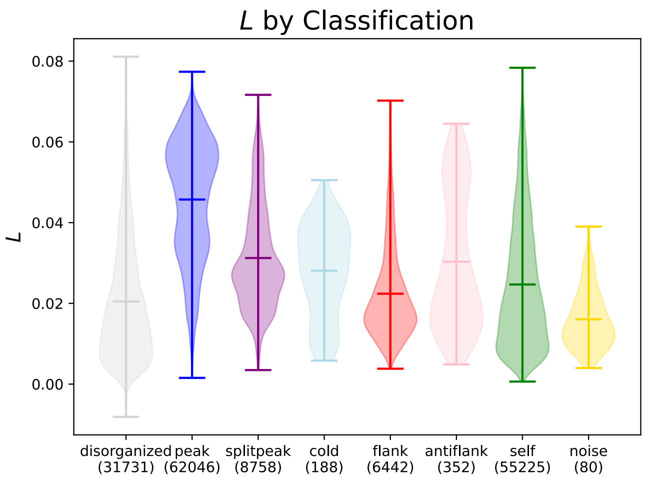

Figure 7. Violin plot of L for each Fourier classification structure across all 11 cloud-resolving models and all five sea surface temperatures. The number represents the frequency of each classification.

organization modes, there are still obvious differences between the most and least organized classifications, with "disorganized" having a noticeably lower average I than other states, while "peak" and "self" have the highest I of the frequently-occurring states. There are also links between the Fourier classifications in RCEMIP-II and the strength of convective organization in RCEMIP-I. Among the six CRMs which participated in both RCEMIP-I and II, two showed average I values greater than 0.8 in `RCE_large300`: SAM-CRM and MESONH. These are precisely the models for which "self" classification is demonstrated in more than 80% of scenes. By contrast, the ICON-CRM `RCE_large300` simulation shows the lowest I (0.65), and is the only model for which `MW_300dT1p25` shows 100% "peak" classification. While the sample size is small, this suggests models which are more organized in the absence of an SST gradient have stronger self-aggregation feedbacks, which are more likely to resist the SST forcing in the mock-Walker simulations and thus more likely to prevent the formation of a "peak" structure.

4.3. Changes in Organization

4.3.1. Changes With Mean SST

We first consider how each of the organization metrics (see Section 4.1 and Appendix A) changes with mean warming (Figure S13 in Supporting Information S1). This can be directly compared against Figure 16 in Wing et al. (2020a), which performed the same analysis on RCEMIP-I. The changes seen in the metrics are numerically fairly large, but still small enough that there are rarely changes between what would be considered "organized" and "disorganized" states.

As in RCEMIP-I, results for the CRMs are indecisive. Of the 55 total combinations of model and metric, 19 show increases in organization with warming, 29 show decreases, and seven show changes which cannot statistically be distinguished from 0. This is not statistically different from randomness according to a χ^2 test. Despite this randomness, correlations between the changes of most pairs of metrics across the CRMs exist. This indicates that for a given model, most metrics agree on how organization changes with warming.

In the GCMs, metrics tend to agree on increases in organization. 26 of the 30 model-metric pairs show increases with warming, including all models for I, L, and V. This consensus that organization increases with mean warming in models with parameterized convection was also seen in RCEMIP-I. Comparing results from CRMs and GCMs continues to show the importance of resolving convection for understanding changes in convective organization with warming.

Treating the Fourier classification as an alternative metric, we can also examine its changes with SST. Figure 8 shows the distribution of the Fourier classifications (described in Section 4.2) for each SST pattern. At small $\langle T \rangle$, peak- and self-organized structures are both very common. As the mean SST is increased, both decrease in frequency while the frequency of disorganized structure increases. The `305dT1p25` simulations most frequently show >2 m/s of wind shear, which favors large-scale disorganization (Section 4.2). These changes in wind shear as the SST changes could contribute to the changes in organization observed across the ensemble here and in all remaining sections of the paper. Flank-type structure is uncommon at all SSTs, but it more frequently occurs with the largest $\langle T \rangle$.

4.3.1.1. Comparison of RCEMIP-I and II

A direct comparison between RCEMIP-I and II is made in Figure 9. Six CRMs and three GCMs participated in both intercomparisons, so these nine shared models are highlighted with larger markers. The main takeaway from the combination of the two projects shows that the cross-CRM spread in the changes in the metrics with warming increased in the presence of an SST gradient. When the SST gradient is present, there is no guarantee that the sign of the change of organization metrics with warming will be the same as the sign of the change without an SST gradient. Most models with simulations in both RCEMIP-I and II show increases in L with warming in RCEMIP-I; the majority show decreases in L with warming in RCEMIP-II. Rather than constraining the models, the forced overturning circulation allows a greater variety of convective structures not seen in RCEMIP-I.

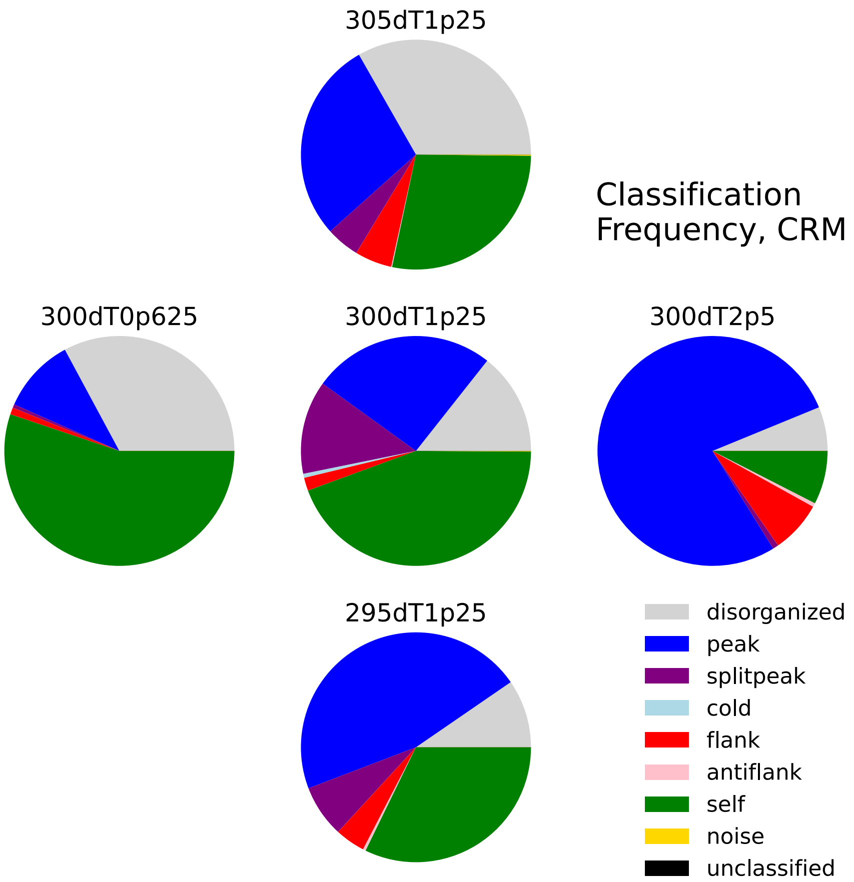

Figure 8. Model-weighted pie charts of the frequency of each Fourier classification for each sea surface temperature (SST) pattern. Each pie is weighted such that each of the 11 cloud-resolving models explains exactly 1/11 of the pie regardless of how many scenes are classifiable. SST patterns with higher mean temperature (large $\langle T \rangle$) are at the top, while those with stronger SST gradients (large ΔT) are to the right.

4.3.2. Changes With SST Gradient

We can similarly look at changes in organization metrics as the SST gradient changes while holding the mean SST fixed. Here, the results decisively favor increases in organization as the SST gradient increases. All 30 combinations of GCM and metric show increases in organization with increased ΔT, although some of these changes are very small (and sometimes non-monotonic if the `300dT1p25` simulation is included as well). While the CRMs do not show unanimity in this increase, 42 of the 55 model-metric pairs show significant increases in organization, with all 11 models demonstrating increases in organization when examining L, O, or V (Figure 10). The mock-Walker simulations are usually more organized than their RCEMIP-I counterparts (not shown).

Figure 8 also shows changes to the Fourier classifications across ΔT by looking along the central row. At small ΔT, self-organized structure dominates, with a large minority of scenes exhibiting disorganized structure. As the SST gradient is increased, peak structure dominates. Flank-type structure continues to be uncommon, but it again more frequently occurs with increases in ΔT. The increased frequency of organized classifications mirrors the increases in the organization metrics as ΔT increases. We also calculated the Fourier classifications for the RCEMIP-I simulations (not shown). For the six CRMs participating in both RCEMIP-I and II, most scenes are classified as "self"-organized, with the vast majority of the remainder classified as "disorganized," continuing the trend seen in Figure 8 toward smaller gradients. Some models which only participated in RCEMIP-I demonstrate frequent "noise" classification: it is unclear whether the large-scale overturning circulation of RCEMIP-II suppresses this small-scale organization or whether this is merely an artifact of model selection.

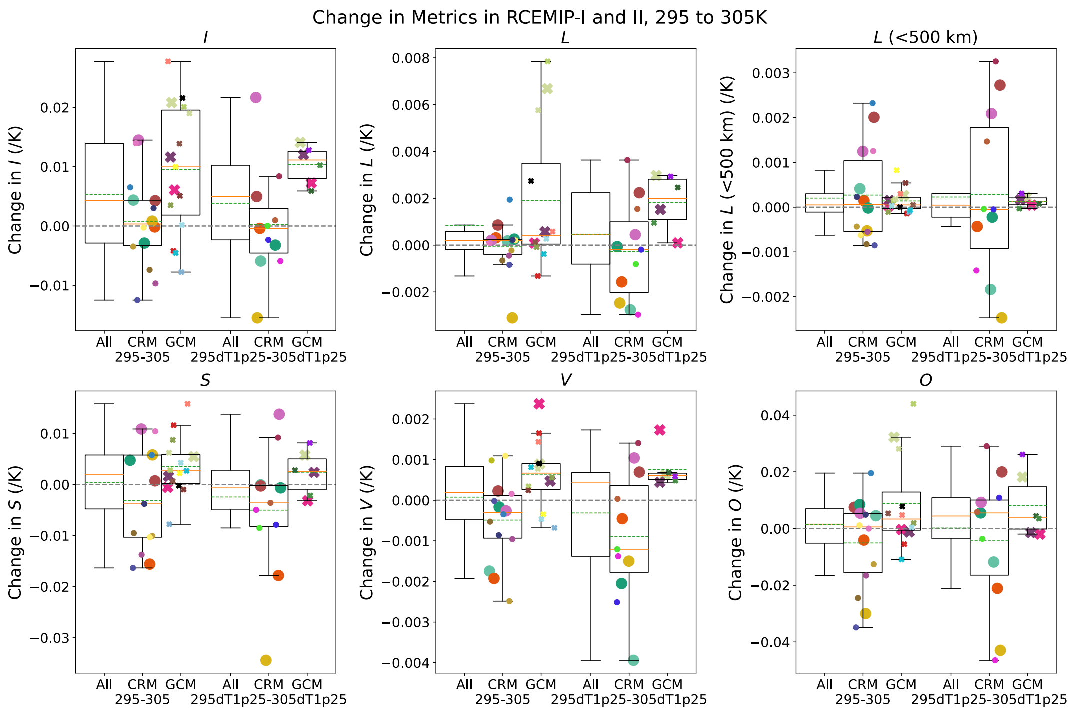

Figure 9. Change in organization metrics between the `RCE_large295` and `RCE_large305` simulations of Radiative-Convective Equilibrium Model Intercomparison Project (RCEMIP)-I and the `295dT1p25` and `305dT1p25` simulations of RCEMIP-II, including L integrated only up to the 500-km scale. Changes are plotted as a per-Kelvin value with a denominator of 10 K. Models which participated in both RCEMIP-I and RCEMIP-II are highlighted with larger markers.

4.3.3. Changes With Nonuniform Warming

Changes in organization metrics can also be examined between four pairs of SSTs in which mean SST and the SST gradient change simultaneously: the "cold increase" case between `MW_295dT1p25` and `MW_300dT2p5`, the "cold decrease" case between `MW_295dT1p25` and `MW_300dT0p625`, the "warm increase" case between `MW_300dT0p625` and `MW_305dT1p25`, and the "warm decrease" case between `MW_300dT2p5` and `MW_305dT1p25`. We would expect the changes in organization metrics across the CRMs to blend the randomness from changing $\langle T\rangle$ with the strong preference for increased organization with increased ΔT. We found this to be true, as across the four SST combinations, most pairs of CRM and metric show the expected sign change from how ΔT changes (not shown). That is, when both $\langle T\rangle$ and ΔT increase, there is a tendency toward increased organization. When $\langle T\rangle$ increases but ΔT decreases, there is a tendency toward decreased organization. However, the change in organization is smaller than that when ΔT changes in isolation. For the GCMs, where the response to uniform warming is biased toward increased organization, the "decrease" cases experience offsetting effects of increased $\langle T\rangle$ and decreased ΔT. The sign of the organizational response appears to depend on the magnitude of the change in ΔT. For the "warm decrease" case, where ΔT decreases by 1.25 K, 18/30 GCM-metric pairs show decreased organization. However, for the "cold decrease" case, where ΔT decreases by only 0.625 K, 23/30 such pairs instead show increased organization. These results emphasize that while there is no consensus in the response of organization to uniform warming, there is general agreement across models in the response of organization to patterned warming, which is a better analogy for real-world tropical warming.

5. The Mock-Walker Hydroclimate and Change

This section explores the hydroclimate of the mock-Walker simulations, including various important climate variables, the behavior of clouds, climate sensitivity, and extreme rainfall.

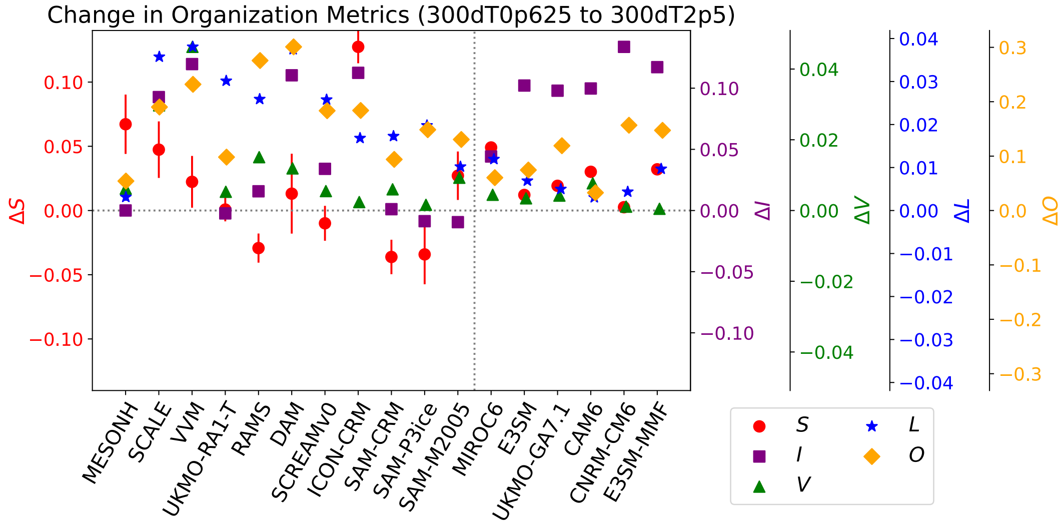

Figure 10. Change in the organization metrics between the `300dT0p625` and `300dT2p5` simulations. 2σ error bars have been plotted for each metric as a vertical line segment through the scatter point, but these are only visible for S.

5.1. Mean Climate Variables

Figure 11 compares several important climate variables between RCEMIP-I and RCEMIP-II for the nine models (6 CRMs, 3 GCMs) which performed both sets of simulations, examining the impact of changes in the SST gradient. A similar plot across changes in the mean SST is given as Figure S14 in Supporting Information S1. We hypothesized that an existence of an SST gradient would, by driving a common forced circulation, constrain the intermodel spread. This is not the case; for many variables, the intermodel spread across the same set of models is similar to or larger in RCEMIP-II than RCEMIP-I. Many trends seen in Figure 11 can be seen as consequences of the increase in the maximum SST within the domain as ΔT is increased. Convective quasi-equilibrium (Emanuel et al., 1994) and the weak temperature gradient approximation (Charney, 1963; Sobel & Bretherton, 2000) together constrain the tropical-mean thermodynamic structure to be near a moist adiabat determined by near-surface conditions where deep convection occurs. The precipitation-weighted SST (PSST) of Fueglistaler et al. (2015) is a simple proxy for this constraint that tracks closely with maximum SST, with a multi-model mean PSST depressed by between 0.24 and 0.40 K from the peak SST for all model sets. Physical mechanisms involving changes in that metric have been linked to several of the climate variables discussed below.

Domain-mean precipitation rate increases with both mean SST (Figure S14a in Supporting Information S1) and the SST gradient (Figure 11a), while net downward TOA radiation decreases with increases in both $\langle T \rangle$ (Figure S14b in Supporting Information S1) and ΔT (Figure 11b). These are both consequences of the increase in longwave cooling of the atmosphere in response to increases in PSST (Williams & Jeevanjee, 2025; S. Zhang et al., 2023) and the constraint on mean precipitation from the atmospheric energy budget (Allen & Ingram, 2002). The intermodel spread in both variables is comparable in RCEMIP-I and RCEMIP-II. Cloud water path slightly increases with $\langle T \rangle$ (Figure S14c in Supporting Information S1) and with ΔT (Figure 11c). The spread is larger in RCEMIP-II when outliers are included. Precipitable water (PW) increases with increases in both $\langle T \rangle$ (Figure S14d in Supporting Information S1) and ΔT (Figure 11d). These changes in CWP and PW are likely consequences of the increased saturation specific humidity in response to the Clausius-Clapeyron equation with a higher maximum SST. Other than an outlier, the spread in PW is smaller in RCEMIP-II for the 300 and 305 K simulations, but larger in the 295 K simulations. The tropospheric lapse rate decreases with increases in $\langle T \rangle$ (Figure S14e in Supporting Information S1) and ΔT (Figure 11e), as the atmosphere's temperature profile moves alongside a warmer moist adiabat. The ice water path (Figure 11f) shows no obvious trend across SST patterns, in part due to outliers. A similar plot including all models–not just those shared between RCEMIP-I and II–is given in Figure S15 in Supporting Information S1. Values for these variables and several other relevant climate variables are given in Table C1 in Appendix C.

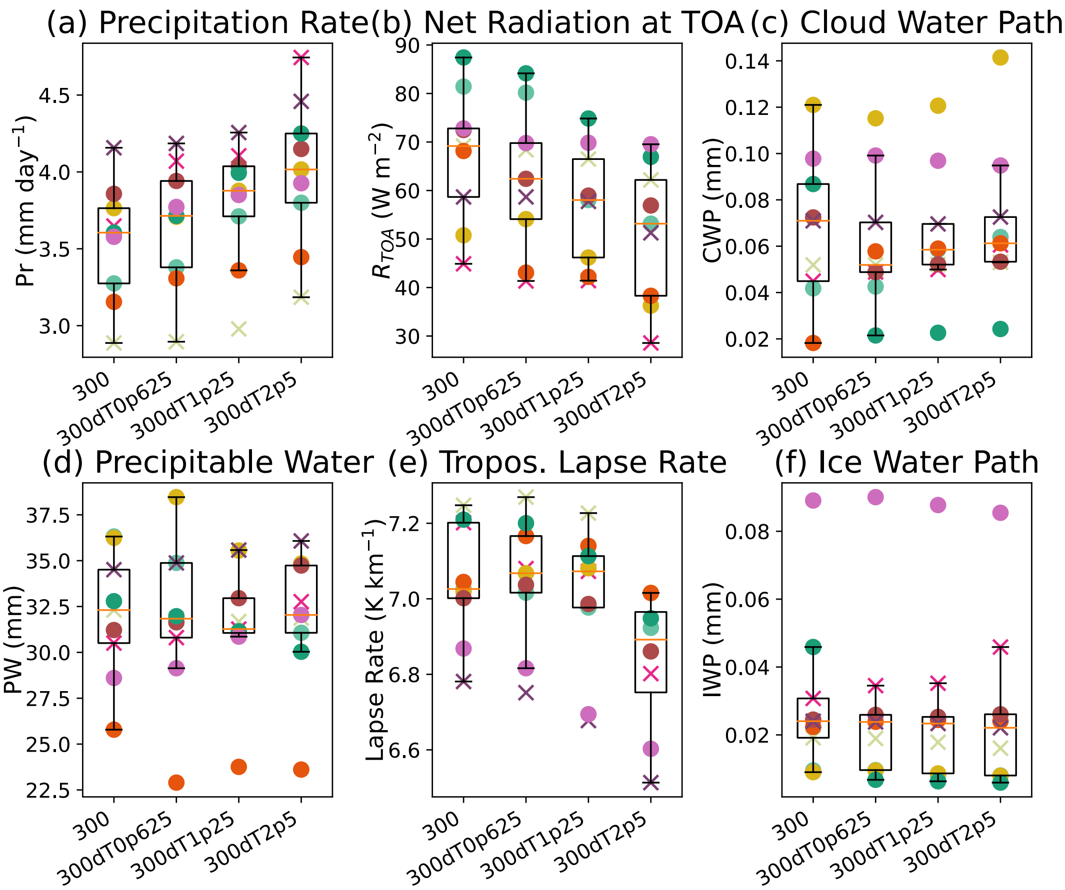

Figure 11. Comparison of several relevant domain-mean atmospheric variables with and without a mock-Walker simulation. Radiative-Convective Equilibrium Model Intercomparison Project-I's `RCE_large300` simulation (leftmost box plot in each panel) includes no Walker circulation, and it is compared against the three mock-Walker simulations with the same mean temperature $\langle T \rangle = 300$ K. Each circle represents a cloud-resolving model while each cross represents a general circulation model. Variables are averaged after day 75.

5.2. Clouds

To investigate the behavior of clouds in the CRMs of RCEMIP-II, we use the International Satellite Cloud Climatology Project (ISCCP) bins to classify grid cells by cloud optical depth (τ) and cloud top pressure (CTP). While three of the GCMs (CNRM-CM6, E3SM and UKMO-GA7.1) provided output from their online ISCCP simulator, the CRMs did not, so we must calculate the cloud histograms offline from the 3D data. For this, we turn to the Approximate ISCCP Simulator (AIS) introduced for RCEMIP-I by Stauffer and Wing (2023). The AIS uses the radiative parameterizations from Fu (1996) and Slingo (1989) and is applied to all of the 6-hourly 3D data in the final 100 days of each CRM. One slight deviation from the ISCCP bins involves the upper limits. While the highest CTP and optical depth on the standard ISCCP bins are 1,000 hPa and 380, respectively, we occasionally see values greater than each of these bounds, so we extend the bins to the surface and to infinite optical depth.

When compiled, the histogram of cloud frequency in each bin for the `300dT1p25` simulations is given in Figure 12, which is analogous to the results from RCEMIP-I's `RCE_large300` simulations shown in Figure 1k of Stauffer and Wing (2024). Qualitatively, the two figures are very similar. RCEMIP-II shows some enhancement of low-level medium-thickness clouds (CTP from 680 to 1,000 hPa, τ from 0.3 to 23) relative to that past work in RCEMIP-I. These clouds are more common over the cooler half of the domain and at least in some models (most notably MESONH, SCREAMv0, and ICON-CRM) they have mean diameters much larger than the grid scale (not shown), indicating that these models may be generating stratocumulus, a cloud type not seen in RCEMIP-I. RCEMIP-II also shows suppression of thinner clouds (CTP from 180 to 800 hPa, τ from 0 to 0.3). RCEMIP-II `300dT1p25` exhibits an average cloud fraction of 73.0%, slightly lower than the 76.0% seen in

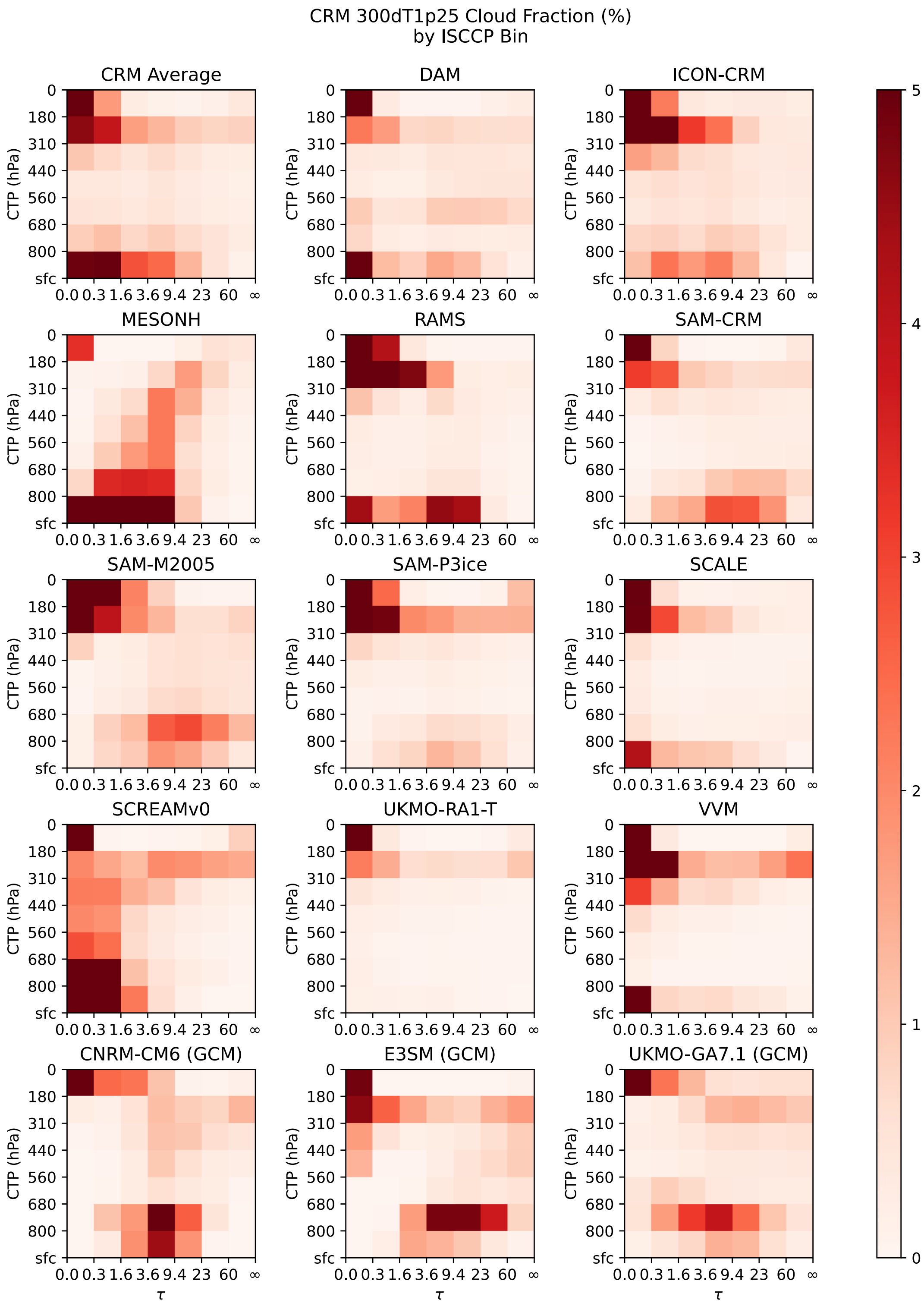

Figure 12. Multimodel International Satellite Cloud Climatology Project histograms for the `300dT1p25` simulations. Grid cells are binned by cloud top pressure and optical thickness (τ). Data are averaged after day 100 for all simulations.

`RCE_large300`. Some differences are to be expected, as the two figures are not based on the same models, so it is unclear if this is a general feature of the mock-Walker simulations or just an artifact of model selection. Results from other simulations are given as Figures S16–S19 in Supporting Information S1.

We examine changes in clouds with warming of the mean SST by comparing `305dT1p25` against `295dT1p25` in Figure 13. While there are some subtle differences in the low-level cloud fields and cloud fraction decreases with warming at most altitudes, the most obvious feature is the dipole between decreasing cloud fraction at a CTP of 180–310 hPa alongside an increase of cloud fraction above this layer. While Stauffer and Wing (2024) did not present this analysis for `RCE_large`, Stauffer and Wing (2023) performed a similar analysis on `RCE_small` and found the same feature. This is best explained as a rise in cloud top height as the troposphere deepens with warming (Hartmann & Larson, 2002). We also find an extremely small increase in total cloud fraction with mean warming, from 73.7% for `295dT1p25` to 73.8% for `305dT1p25`. This change is insignificant, and the lack of a trend is further suggested by how the intermediate `300dT1p25` simulations show a lower cloud fraction than either. This is unlike Stauffer and Wing (2023), who found a slight decrease in total cloud fraction with warming. The near lack of a change in total cloud fraction is caused by small but offsetting changes to low (CTP > 680 hPa) and high (CTP < 440 hPa) cloud fraction: between the `295dT1p25` and `305dT1p25` simulations, low cloud fraction decreases from 23.8% to 22.8% while high cloud fraction increases from 44.1% to 46.7%.

We also look at changes to the ISCCP histograms due to changes in the SST gradient at a given mean SST in Figure 14. Two features immediately stand out. The first is a decrease in high clouds, consistent with less convective detrainment in a more stable upper troposphere (Bony et al., 2016). This decrease, predominantly seen in thin clouds, occurs despite a slight increase in deep, thick clouds in the upper-right section of the figure in some models. This indicates that additional mechanisms beyond the stability-iris hypothesis also influence the cloud distribution. We speculate that in the simulations with higher ΔT and larger and drier dry regions, spreading cirrus clouds may more rapidly evaporate as they encounter drier air. Additionally, the high-ΔT simulations tend to have fewer distinct moist regions and thus a smaller moist-dry region interface, implying a smaller area of the transition regions where we would expect spreading anvils.

The second notable feature is an increase in lower-level clouds, most concentrated at a CTP of 680–800 hPa and τ from 9.4 to 23. This is probably in part due to an increase in stratocumulus in the presence of a cooler cool pool, though the increase in cloud fraction extends far beyond the regions of the ISCCP diagram where one would expect to find stratocumulus. Increases in ΔT show a decrease in total cloud fraction, from 75.2% in `300dT0p625` to 72.8% in `300dT2p5`. This is driven by a decrease in high cloud fraction from 48.9% to 43.7%, while low cloud fraction increases from 21.8% to 23.4%.

5.3. Climate Feedbacks

The set of SST distributions chosen for RCEMIP-II allows investigation of what happens in global warming scenarios where the SST gradient increases, remains constant, or decreases. This is analogous to the real-world situation in which a non-uniform pattern of warming influences climate feedbacks. In particular, it is critical whether warming is enhanced in the warmest, deep convecting regions, or in colder, subsiding regions (Andrews et al., 2022; Fueglistaler & Silvers, 2021). In Figure 15, this is done with a final state of the `305dT1p25` simulation. Increasing ΔT starts from `300dT0p625`, constant ΔT from `300dT1p25`, and decreasing ΔT from `300dT2p5`. Moving from weakening ΔT to strengthening ΔT, the Cess-type climate feedback parameter λ decreases by approximately 2 W/m^2. For weakening ΔTs, λ is actually positive in many models, indicating an unstable climate. The possibility of a local runaway greenhouse state was also noted by Schneider et al. (2019), who found higher climate sensitivities after stratocumulus breakup at high CO_2 levels led to a weaker gradient between their subtropical and tropical domains.

Similar sensitivity to ΔT occurs when considering warming from the `295dT1p25` simulation as the initial state to each of the simulations at $\langle T \rangle = 300$ K (not shown). The distribution of λ in RCEMIP-I is generally similar to that in RCEMIP-II for the case of warming with constant ΔT, though RCEMIP-II has an even larger intermodel spread (Becker & Wing, 2020; Wing et al., 2020a).

This overall behavior is largely consistent with expectations from literature on the pattern effect in which enhanced "La Niña-like" warming in regions of deep convection (strengthened ΔT) leads to lower climate sensitivity (more negative λ). Prior work has attributed this to a stronger negative lapse rate feedback due to increased stability and a less positive or more negative low cloud feedback due to increases in low cloud cover in the cold regions (Andrews & Webb, 2018; Ceppi & Gregory, 2017; Dong et al., 2019; Zhou et al., 2016); future work will investigate whether the same mechanisms are responsible in the RCEMIP-II simulations.

10.1029/2026MS005781

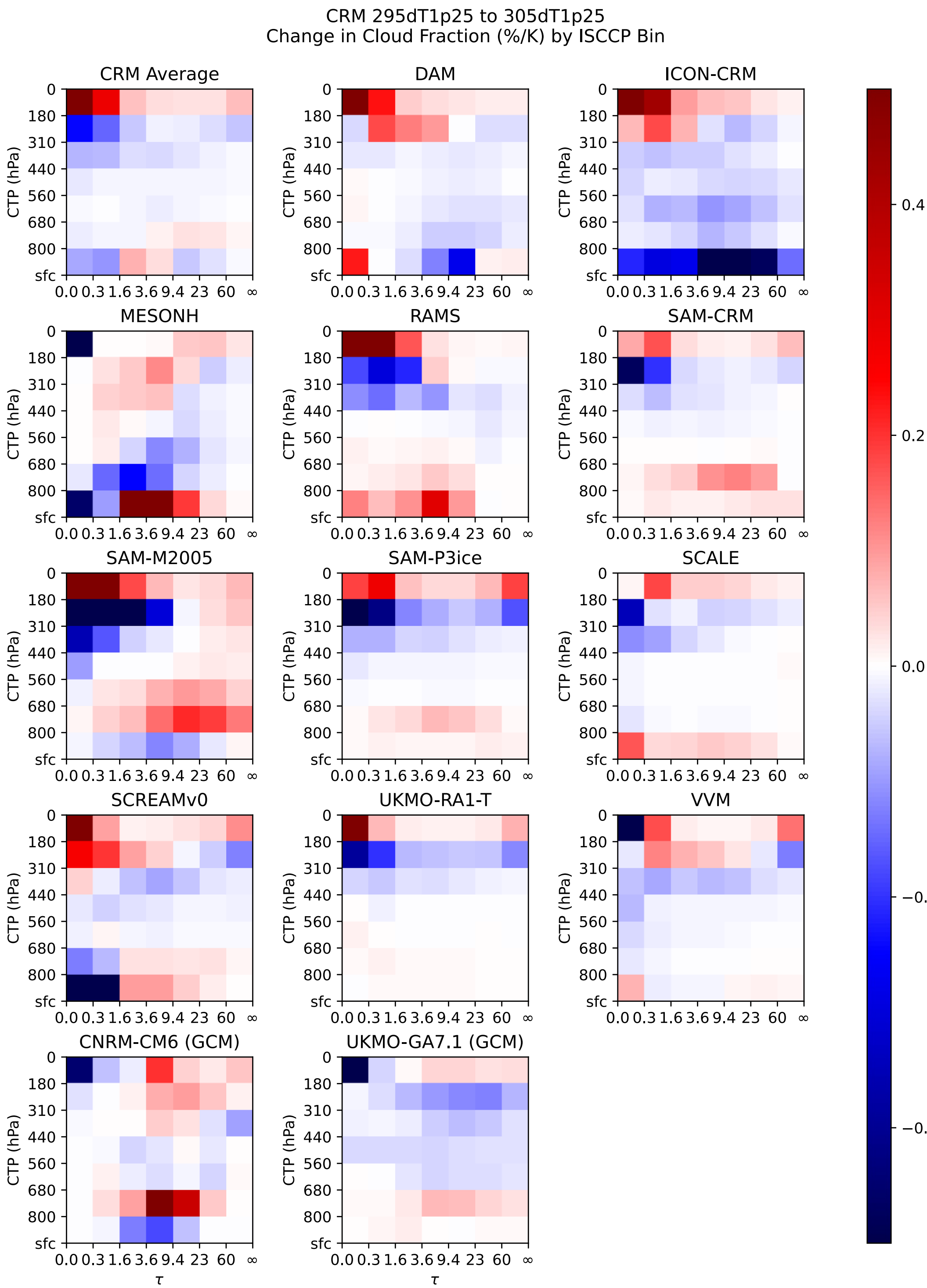

Figure 13. Difference between the multimodel International Satellite Cloud Climatology Project histograms for the `305dT1p25` and `295dT1p25` simulations, given as an absolute %/K change. Plots are averaged after the first 100 days of simulation.

5.4. Extreme Rainfall

In RCEMIP-I, O'Donnell and Wing (2024) found that while extreme precipitation (P) increases with warming approximately as the Clausius-Clapeyron relation with SST, deviations from this scaling exist. These deviations

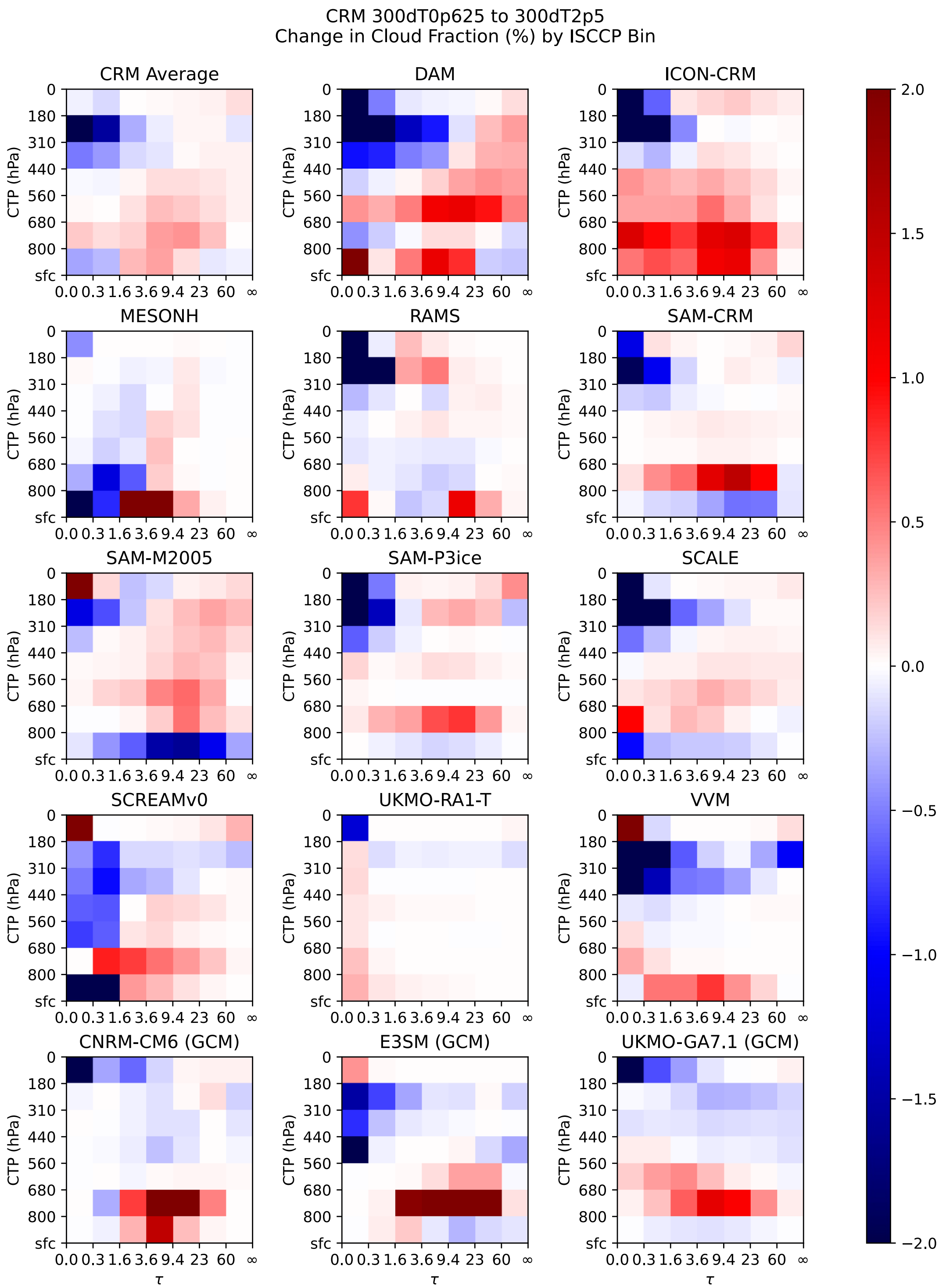

Figure 14. Difference between the multimodel International Satellite Cloud Climatology Project histograms for the `300dT0p625` and `300dT2p5` simulations. Plots are averaged after the first 100 days of simulation.

tend to be correlated with changes in convective organization, measured with I. Here, we retrace the important stages of that analysis to determine whether the same holds true in the presence of an SST gradient (Section 5.4.1) or with changes in the SST gradient (Section 5.4.2). The purpose of this paper is to compare RCEMIP-I and II, so we emphasize the similarities between results here and O'Donnell and Wing (2024). We refer to that paper and references therein for a more thorough description of physical mechanisms that impact extreme rainfall, and

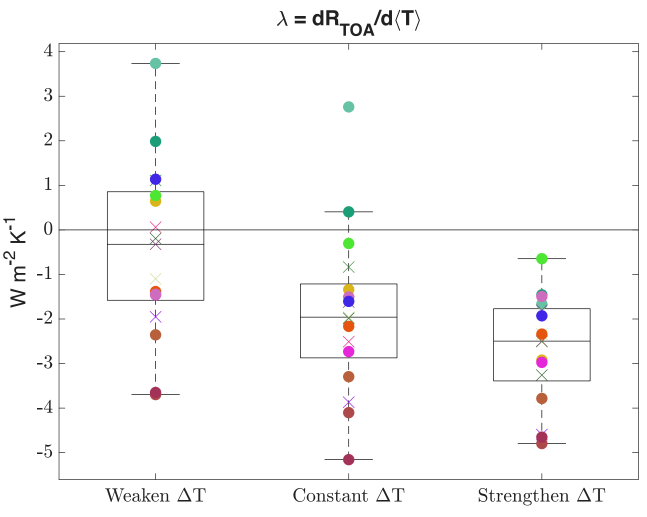

Figure 15. Cess-type climate feedback $\lambda = \mathrm{dR_{TOA}}/\mathrm{d}\langle\mathrm{T}\rangle$ as calculated with a final state of the `305dT1p25` simulation. For the "Weaken ΔT" case, climate sensitivity is calculated between `300dT2p5` and `305dT1p25`. For the "Constant ΔT" case, climate sensitivity is calculated between `300dT1p25` and `305dT1p25`. For the "Strengthen ΔT" case, climate sensitivity is calculated between `300dT0p625` and `305dT1p25`.

elaborate here on a mechanism only present with an SST gradient. As in O'Donnell and Wing (2024), we define extreme rainfall as any event where hourly rainfall in a 15-km square region exceeds its 99.9th percentile, and P as the mean rainfall rate during such events.

5.4.1. Changes in Extreme Rainfall With Mean SST

Figure 16a shows the changes in P and I between the `295dT1p25` and `305dT1p25` simulations, along with the correlation between those changes. A significant correlation with $r = 0.75$ is found between the two. Figure S20a in Supporting Information S1 shows a map of this correlation coefficient, recalculated when redefining P at many scales between grid-scale (3 km) and 90 km spatial coarsening and between 1- and 48-hr accumulation. As in O'Donnell and Wing (2024), we find statistically significant correlations at sufficiently large spatial scales, though the correlations do not reach significance if coarsening only in time. Similar results are found when other organization metrics are used in place of I (not shown). As in O'Donnell and Wing (2024), changes in organization and extreme rainfall with mean warming are linked through mechanisms related to updraft magnitude and precipitation efficiency, as quantified by the scaling first introduced by O'Gorman and Schneider (2009) and Muller et al. (2011). We also find one new mechanism for enhancing extreme rainfall where more organized scenes demonstrating "peak"-type structure generate their extreme rainfall over warmer SSTs than the domain average, allowing an additional thermodynamic contribution to extreme rainfall. This is more thoroughly described in Text S2 and Figures S21 and S22 in Supporting Information S1.

5.4.2. Changes in Extreme Rainfall With the SST Gradient

We can perform a similar analysis on changes in extreme rainfall with changes in the SST gradient while holding the mean SST constant to examine how the forced circulation impacts extreme rainfall. Figure 16b shows the correlation between the change in P and the change in I between the `300dT0p625` and `300dT2p5` simulations, again finding a significant correlation with $r = 0.62$. Figure S20b in Supporting Information S1 shows the map of this correlation coefficient across scales. Trends are less clear-cut than for the change in mean SST, as while the correlations generally strengthen with increasing temporal scale, they weaken with increased area. Results when ΔI is replaced by other metrics are also inconsistent with each other (not shown). A mechanism analysis (Muller et al., 2011; O'Gorman & Schneider, 2009) suggests that while increased organization in response to an increased SST gradient still increases extreme rainfall through the precipitation efficiency and thermodynamic mechanisms, the link through updraft magnitude seen for the response to mean warming is lost and may reverse sign. More details on this are given in Text S2, Figures S21 and S23 in Supporting Information S1.

6. Discussion and Conclusions

RCEMIP-I was unique in its accessibility to an exceptionally broad variety of model types, including GCMs, CRMs, SCMs, LESs, and GCRMs. While RCEMIP-II does not encompass quite as broad a menagerie of models, it moves an important step toward more realistic boundary conditions and opens new research questions to analysis across a broad ensemble of idealized simulations. This paper provides a first look at some of those questions.

The first scientific objective of RCEMIP-I was to determine the response of clouds to warming and the climate sensitivity. We find that when moving from the coldest to the warmest simulations in RCEMIP-II, high clouds get somewhat higher while the overall cloud fraction decreases slightly in the multi-model average. However, the nature of these changes is not universal across models, so even when ΔT is held constant models show a net climate feedback anywhere from strongly negative to noticeably positive. Unlike RCEMIP-I, RCEMIP-II allows an idealized climate sensitivity with a pattern effect to be estimated, finding that if ΔT increases with warming, the net climate feedback is much more negative (lower climate sensitivity). Many models show a positive climate

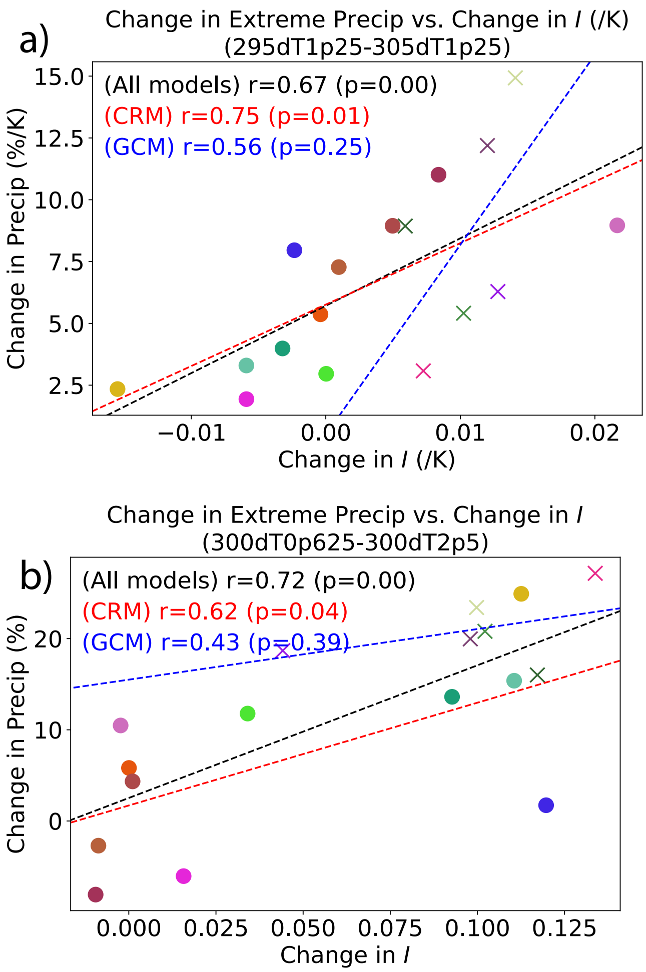

Figure 16. Change in extreme precipitation vs. the change in organization index, as calculated between (a) the `295dT1p25` and `305dT1p25` simulations, and (b) the `300dT0p625` and `300dT2p5` simulations. Each circle represents a cloud-resolving model within the ensemble, while each cross represents a general circulation model.

feedback (extremely high, unstable climate sensitivity) if the SST gradient is instead weakened. Understanding the pattern effect is important because real-world climate warming is non-uniform.

The second objective deals with the dependence of convective aggregation and circulation on temperature. For RCEMIP-II, one parallel question involves the behavior of organization metrics across changes in both the mean SST and its gradient. With warming in the presence of an SST gradient, we find very similar results to RCEMIP-I. While GCMs largely show increases in organization with warming, CRMs show mixed results, with some individual models showing increases by all tested metrics, others showing decreases across all metrics, and a plurality showing mixed results when different metrics are used. No consensus on the change in organization with mean warming in CRMs can be found either here or in RCEMIP-I (Wing et al., 2020a). However, we do find that a majority of models show increased organization according to most metrics as the SST gradient is increased, either on its own or in concert with mean warming. We also introduce a new method for quantifying the spatial structure of convection via a Fourier decomposition of the CRH field, which can be seen as complementary to conventional organization metrics.

The third objective involves the robustness of the RCE state. Another parallel to the previous point involves the interaction of circulations driven by self-aggregation with the SST-forced circulation and whether a given structure should be expected across simulations. A reasonable null hypothesis is that the forced circulation would provide a common base structure across models (Wing et al., 2024). However, if anything we find the opposite is true: a wider variety of spatiotemporal structures exists in RCEMIP-II than in RCEMIP-I. Even for the same SST pattern, we find that some models prefer to cluster their convection at the maximum SST, others prefer to organize their convection where the SST gradient is maximized, and still others exhibit a more RCEMIP-I-like self-organized structure. We find that most individual modes of convective organization become less common as the mean SST is increased as disorganized scenes become more frequent, while we see a distinct shift from self-organized structures to warm pool-centered structures as the SST gradient is increased. As a consequence of the wide range of convective structures, the intermodel spread in mean climate variables is *not* reduced in RCEMIP-II compared to RCEMIP-I. Future approaches to more strongly constrain a common structure could include prescribing the large-scale circulation itself, nudging the domain-mean horizontal wind to 0 to prevent spontaneous shear development, or including rotation, all of which provide additional dynamical controls.

These early results from RCEMIP-II re-emphasize the importance of representation of convection, microphysics, turbulence, and dynamical core in controlling tropical clouds and circulation. They provide insight into the interaction of intrinsic self-aggregation of convection, driven by internal radiative-convective feedbacks, with externally forced circulations. They also reveal that an SST gradient, at least of the quasi-realistic magnitudes used here, is not on its own effective at constraining model behavior. However, it does introduce new phenomena compared to those present in RCEMIP-I. The RCEMIP-II simulations exhibit more low clouds than in RCEMIP-I, due to the possible presence of stratocumulus in the cold regions. Increases in convective organization with warming enhance the increase in precipitation extremes as in RCEMIP-I, but with an additional thermodynamic contribution due to a shift of convection toward the warm SSTs. The suite of simulations with varying $\langle T \rangle$ and ΔT permit the first-ever demonstration of the pattern effect in an ensemble of models with explicit convection. Ongoing work will extend the initial results presented here to (a) examine mechanisms driving cross-model differences in circulation strength and structure and (b) investigate mechanisms for the pattern effect on climate sensitivity and their consistency with simulations further up the model hierarchy. Many other research directions are possible with the combined RCEMIP-I and RCEMIP-II public data sets.

Appendix A: Organization Metrics

To quantify the degree of convective organization with a simple number, we rely on several organization metrics. For RCEMIP-I, three metrics were examined:

- Subsidence fraction (S or f_{sub}): the fraction of the domain for which the daily-averaged 100-km scale 500-hPa vertical velocity is descending. A value greater than 0.5 suggests some degree of convective organization.
- Variance of column relative humidity (V or σ^2_{CRH}): the spatial variance of CRH, defined as the ratio of precipitable water to saturation precipitable water. There is no specific value which delimits disorganized from organized convection.
- The organization index (I or I_{org}) (Tompkins & Semie, 2017): a metric based on the distribution of nearest-neighbor distributions between convective cells. A value of 0.5 denotes randomly distributed convection while a value of 1 denotes totally clustered convection.

These three metrics were implemented in the same manner here as in RCEMIP-I (Wing et al., 2020a), with the first 75 days of the simulations excluded and with "convective cells" defined by an OLR below 173 W m^{-2} for the I calculation. As in Wing et al. (2020a), four-point connectivity was used to define convective entities for both CRMs and GCMs, and in the GCMs all metrics were calculated over the band from 27°S to 27°N. Additional metrics have been developed since the release of RCEMIP-I, and we chose to implement two of these:

- L_{org} (or L): a metric based on the full distribution of paired distances between convective cells (Biagioli & Tompkins, 2023). A value of 0 is characteristic of random convection, while a more positive value shows stronger organization. As L is calculated as an integral over a range of these distances from 0 to the domain scale, limiting the integral to a different range can explicitly denote organization at specific scales.
- The Organization Index based on Distance and Relative Area (O or OIDRA): a metric similar to L in that it accounts for the full distribution of paired distances, but also accounts for the size of individual convective cells and clusters (Mandorli & Stubenrauch, 2024). Its definition requires assuming a length scale, which we set to constrain O between 0 and 1, but there is no threshold value separating "organized" and "disorganized" convection.

Appendix B: Definition of the Fourier Classification

To calculate the Fourier classifications discussed in Section 4.2, we first take an average of the CRH across the short dimension of the long-channel CRM domain. We then subtract away the full-domain average of CRH to remove the constant term of the Fourier series. This results in a spatial anomaly of CRH as a function of time, $\mathrm{CRH}'(t,x)$. Calculating the Fourier series,

$$\mathrm{CRH}'(t,x) = \sum_{k=1}^{n_x} a_k(t)\cos\frac{2\pi kx}{L} + \sum_{k=1}^{n_x} b_k(t)\sin\frac{2\pi kx}{L} \tag{B1}$$

where n_x is the number of grid cells in the domain length and $a_k(t), b_k(t)$ are coefficients as a function of time.

Notice that as the SST distribution is proportional to $-\cos\frac{2\pi kx}{L}$ for $k = 1$, $-a_1(t)$ describes the amount of CRH variance correlated to the SST distribution. Thus, we define $P(t) = a_1(t)^2$ as the "peak" variance function. Also note that the magnitude of the gradient of the SST distribution, $|\sin\frac{2\pi kx}{L}|$, has an extremely similar two-peaked structure to the second Fourier mode, so $-a_2(t)$ approximately represents the CRH distribution explained by the SST gradient. We thus define $F(t) = a_2(t)^2$ as the "flank" variance function. Other large-scale structures in the CRH field are most likely explained by self-aggregation. Here, we assume any other structure with a length scale ≥1000 km is self-aggregated, and with a ∼6,000-km-long domain this is explained by Fourier modes up to $n = 6$. Thus, we define $S(t) = \sum_{k=3}^{6} a_k(t)^2 + \sum_{k=1}^{6} b_k(t)^2$ as the "self" variance function. All remaining variance is assumed to be small-scale noise, so the function $N(t) = \sum_{k=7}^{n_x} a_k(t)^2 + \sum_{k=7}^{n_x} b_k(t)^2$ is defined as the "noise" variance function.

To convert these into a discrete classification of convection, we compare $P(t), F(t), S(t)$, and $N(t)$.

- If the total zonal CRH variance $V(t) = \sigma^2_{\mathrm{CRH}}(t) < 0.02$, we describe the scene at time t as "disorganized," depicted by gray coloring in figures.
- If $P(t)$ is the largest of the four variance functions at time t (i.e., $P(t) > F(t), S(t), N(t)$), then high CRH occurs at the region of highest SST and we describe the scene as "peak" organization (blue).
- If $F(t)$ is the largest of the four variance functions, then high CRH occurs at the locations of maximum SST gradient and we describe the scene as "flank" organization (red).
- If $S(t)$ is the largest of the four variance functions, then high CRH occurs in a small number of distinct clusters largely independent of the SST and we describe the scene as "self" organization (green).
- If $N(t)$ is the largest of the four variance functions, then CRH has significant variance but does not form large moist and dry regions, so we describe the scene as "noise" organization (yellow).

The 0.02 CRH variance threshold for "organized" versus "disorganized" is arbitrary but designed to capture the initial evolution from spatially uniform to organized convection (Figure 5). However, as organization in terms of CRH variance exists on a continuum from fully disorganized to fully organized this "disorganized" category may be more accurately interpreted as identifying the least organized scenes. These may still exhibit some signs of convective organization, such as the SAM-P3ice `MW_300dT1p25` simulation around day 160 where CRH variations become more subtle (Figure 5).

Some special cases still appear and require additional classification, though they are rarer.

- Both "peak" and "flank" structures have a sign dependence on a_1 and a_2, respectively. If a_1 is positive, the CRH field is anticorrelated with the SST (high CRH occurs at the region of lowest SST). As such, we classify scenes where $P(t)$ is greatest but $a_1(t)$ is positive as a "cold" structure (light blue). Similarly, cases where $F(t)$ is greatest but $a_2(t)$ is positive is called an "antiflank" structure, in which high CRH occurs at both the highest and lowest SSTs (pink).
- Some scenes are classified as "peak" but still have a distinct minimum of CRH at the center of the domain. If the positive CRH anomaly averaged over the middle twelfth of the domain (between $11L/24$ and $13L/24$) is less than half of that averaged over the middle third of the domain excluding the middle twelfth (between $L/3$ and $2L/3$), we define a scene as "splitpeak" (purple).

An example of how this methodology is performed is given in Figure B1 for the SAM-CRM `MW_295dT1p25` simulation, which exhibits a variety of structures over time. Initially, a single moist region develops over the

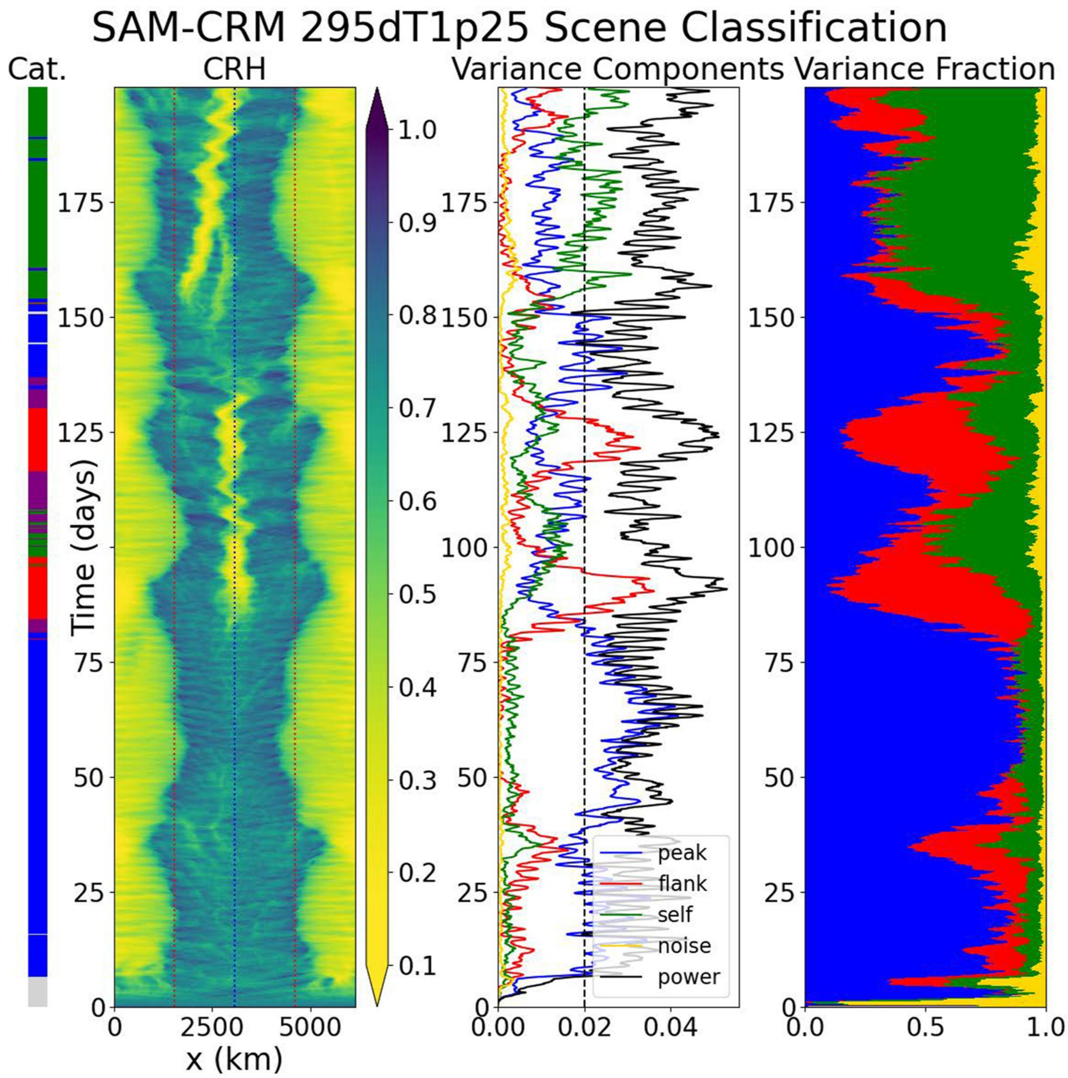

Figure B1. Example of the Fourier classification for the SAM-CRM `295dT1p25` simulation. Blue represents "peak" structure, red represents "flank," green represents "self," and yellow represents "noise." The purple "splitpeak" and gray "disorganized" classifications can also be seen in the categorization ("Cat.") column. On the column relative humidity Hovmoller diagram, the blue dotted line shows the location of the maximum sea surface temperature (SST) while the red dotted lines mark the location of the maximum SST gradient.

warmest SSTs, so after "disorganized" scenes during the first several days of spin-up the simulation is classified as "peak." This remains the classification despite expansion and contraction of the moist region until the spontaneous formation of a central dry region around day 80, leading to "splitpeak" and "flank" classifications until this dry region dissipates near day 135. Near day 150, two separate dry regions develop, leading to order-3 Fourier modes dominating and leading to a "self" classification. While these two regions merge around day 170, the resulting pattern is offset several hundred kilometers left of the SST peak, with the asymmetric order-1 mode and other large-scale modes combining to keep the "self" classification.

This methodology as written does not apply well to the GCMs: aggregation on the zonal dimension causes issues with any obvious adaptation to the domain. If the $54° \times 4°$ slice matching the size of the CRM domain discussed in Section 2 is chosen, it may not intersect a moist region at all. Alternatively, if a zonal average of the full domain is chosen, moist and dry regions along the warm band are averaged together, missing a large fraction of the CRH variance. Repeating the analysis for many 4°-wide slices around the domain would fail to capture the zonal self-aggregation due to treating each slice independently, and would result in frequent "disorganized" classifications even for the dry slices of a well-organized scene. This underscores the need for a different method to classify organizational structure in the GCMs.

Appendix C: Domain-Mean Statistics

Table C1 contains domain-mean statistics for each of the `300dT1p25` simulations, averaged after day 75, as well as the ensemble mean and standard deviation. F_{net} is the net energy imbalance of the atmosphere. R_{TOA} is the net energy imbalance into the top of the atmosphere. Q_{OCN} is the implied oceanic heat uptake. R_{net} is the column net radiative flux convergence. OLR and ASR are the top-of-atmosphere outgoing longwave radiation and absorbed solar radiation, respectively. LHF and SHF are the surface latent and sensible heat fluxes into the atmosphere. PW is the total precipitable water. Precip is the precipitation rate. LWP and IWP are the liquid and ice water paths of the atmosphere.

Table C1
Domain-Mean Statistics for Each of the `300dT1p25` *Simulations, Averaged After Day 75, As Well As the Ensemble Mean and Standard Deviation*

Model	F_{net} (W m^{-2})	R_{TOA} (W m^{-2})	Q_{OCN} (W m^{-2})	R_{net} (W m^{-2})	OLR (W m^{-2})	ASR (W m^{-2})	LHF (W m^{-2})	SHF (W m^{-2})	PW (mm)	Precip (mm day^{-1})	LWP (mm)	IWP (mm)	Lapse rate (K km^{-1})
DAM	7.09	58.04	50.95	−115.54	282.62	340.66	109.42	13.21	31.1	3.7	0.050	0.008	−6.98
ICON-CRM	0.61	46.19	45.58	−116.58	268.68	314.87	103.14	14.05	35.6	3.9	0.112	0.009	−7.08
MESONH	0.18	42.20	42.39	−117.21	280.52	322.72	105.43	11.59	23.8	3.4	0.035	0.024	−7.14
RAMS	0.77	61.65	60.88	−108.92	265.46	327.11	98.37	11.32	37.3	3.4	0.020	0.039	−5.29
SAM-CRM	3.01	58.94	55.94	−122.72	278.00	336.94	116.76	8.96	33.0	4.0	0.027	0.025	−6.99
SAM-M2005	3.52	65.65	62.13	−113.51	264.02	329.67	110.09	6.95	34.9	3.8	0.059	0.008	−6.33
SAM-P3ice	3.36	76.70	73.34	−111.90	266.94	343.64	106.09	9.17	31.6	3.7	0.025	0.122	−6.94
SCALE	2.72	74.84	72.12	−121.45	279.93	354.77	112.78	11.39	31.1	4.0	0.016	0.006	−7.11
SCREAMv0	1.01	83.81	84.82	−98.39	270.67	354.49	89.71	7.68	28.6	3.1	0.013	0.093	−7.13
UKMO-RA1-T	0.05	69.84	69.79	−118.57	286.20	356.03	110.30	8.32	30.9	3.9	0.009	0.088	−6.69
VVM	3.87	81.60	77.73	−104.79	255.20	336.80	100.16	8.49	35.4	3.5	0.037	0.116	−5.38
CAM6	0.03	66.48	66.51	−98.44	261.64	328.12	86.23	12.18	31.7	3.0	0.034	0.018	−7.23
CNRM-CM6	1.17	41.42	40.24	−123.10	272.91	314.32	112.86	11.41	31.3	4.1	0.015	0.035	−7.07
E3SM	0.11	40.54	40.43	−126.61	282.58	323.12	117.38	9.33	33.3	4.1	0.104	0.008	nan
E3SM-MMF	0.37	47.44	47.08	−118.92	270.54	317.98	113.37	5.92	37.6	3.9	0.090	0.035	nan
MIROC6	0.36	50.71	50.35	−113.96	267.57	318.27	107.90	6.42	31.6	3.7	0.062	0.022	−7.38
UKMO-GA7.1	0.18	57.76	57.94	−128.92	275.32	333.07	123.10	5.64	35.6	4.3	0.046	0.023	−6.68
Full Mean	1.67	60.22	58.72	−115.27	272.28	332.51	107.24	9.53	32.6	3.7	0.044	0.040	−6.76
Full St. Dev.	1.90	13.70	13.34	8.52	8.28	13.41	9.29	2.50	3.3	0.3	0.031	0.038	0.61
CRM Mean	2.38	65.41	63.24	−113.60	272.57	337.97	105.66	10.10	32.1	3.7	0.037	0.049	−6.64
CRM St. Dev.	2.02	12.99	12.99	6.94	9.09	13.06	7.22	2.22	3.6	0.3	0.028	0.044	0.66
GCM Mean	0.37	50.72	50.43	−118.32	271.76	322.48	110.14	8.48	33.5	3.8	0.058	0.024	−7.09
GCM St. Dev.	0.38	9.12	9.40	10.15	6.49	6.44	11.66	2.64	2.3	0.4	0.031	0.009	0.26

Conflict of Interest

The authors declare no conflicts of interest relevant to this study.

Availability Statement

The standardized RCEMIP data is hosted by the German Climate Computing Center (DKRZ). RCEMIP-I data is publicly available online at http://hdl.handle.net/21.14101/d4beee8e-6996-453e-bbd1-ff53b6874c0e (Wing et al., 2020b). RCEMIP-II data is publicly available online at http://hdl.handle.net/21.14101/b2dc0b0d-fa7e-4149-af65-a8d831390427 (Wing et al., 2025). Code and derived data sets used to generate the results and figures used in this paper were uploaded to a Zenodo repository at https://doi.org/10.5281/zenodo.18318091 (O'Donnell & Wing, 2026).

Acknowledgments

We thank all RCEMIP-I contributors. This work used resources of the Deutsches Klimarechenzentrum (DKRZ) under project ID mh1090, and we thank Karsten Peters for his assistance. We also thank two anonymous reviewers for constructive comments that improved the paper. GLO and AAW are supported by NSF Grant AGS-2140419. KAR and LGS are supported by NSF Grant AGS-2327958. GLO, AAW, KAR, and LGS acknowledge high-performance computing support from the Derecho system (Computational and Information Systems Laboratory, 2023) provided by the NSF National Center for Atmospheric Research (NCAR), sponsored by the National Science Foundation. GD and KS are supported by the German Research Foundation (DFG) under Grant HO 6588/3-1. Computer resources for Meso-NH simulations were allocated by GENCI (project 0111437). GL and SCV are supported by INCUS, a NASA Earth Venture Mission, funded by NASA's Science Mission Directorate and managed through the Earth System Science Pathfinder Program Office under contract number 80LARC22DA011. MIROC6 simulations were performed on the Earth Simulator at JAMSTEC. Computing resources for RAMS simulations were provided by the NASA High-End Computing (HEC) Program through the NASA Advanced Supercomputing (NAS) Division at AMES Research Center. SO received funding from the European Research Council (ERC) Synergy Grant "Understanding and Modeling the Earth System with Machine Learning (USMILE)" under the Horizon 2020 research and innovation programme (Grant 855187). SAM-P3ice simulations were performed with computational resources from the Cooperative Institute for Modeling the Earth System and were funded by award NA23OAR4320198 from the National Oceanic and Atmospheric Administration, U.S. Department of Commerce. Computational resources for running SCALE were the supercomputer Fugaku provided by the RIKEN R-CCS through the HPCI System Research project (Project ID: hp240106). PGH acknowledges funding from the UK Natural Environment Research Council for the CIRCULATES project (Grant NE/T006315/1). This work was performed under the auspices of the U.S. Department of Energy by Lawrence Livermore National Laboratory under Contract DE-AC52-07NA27344. Peter Bogen schutz is supported by the Atmospheric System Research program, Tying in High Resolution E3SM with ARM Data (THREAD) project (SCW1800).

References

Allen, M. R., & Ingram, W. J. (2002). Constraints on future changes in climate and the hydrologic cycle. *Nature*, *419*(6903), 228–232. https://doi.org/10.1038/nature01092

Andrews, T., Bodas-Salcedo, A., Gregory, J. M., Dong, Y., Armour, K. C., Paynter, D., et al. (2022). On the effect of historical SST patterns on radiative feedback. *Journal of Geophysical Research (Atmospheres)*, *127*(18), e2022JD036675. https://doi.org/10.1029/2022JD036675

Andrews, T., & Webb, M. J. (2018). The dependence of global cloud and lapse rate feedbacks on the spatial structure of tropical Pacific warming. *Journal of Climate*, *31*(2), 641–654. https://doi.org/10.1175/JCLI-D-17-0087.1

Back, L. E., & Bretherton, C. S. (2009a). On the relationship between SST gradients, boundary layer winds, and convergence over the tropical oceans. *Journal of Climate*, *22*(15), 4182–4196. https://doi.org/10.1175/2009JCLI2392.1

Back, L. E., & Bretherton, C. S. (2009b). A simple model of climatological rainfall and vertical motion patterns over the tropical oceans. *Journal of Climate*, *22*(23), 6477–6497. https://doi.org/10.1175/2009JCLI2393.1

Becker, T., & Wing, A. A. (2020). Understanding the extreme spread in climate sensitivity within the Radiative-Convective Equilibrium Model Intercomparison Project. *Journal of Advances in Modeling Earth Systems*, *12*(10), e2020MS002165. https://doi.org/10.1029/2020MS002165

Beucler, T., & Cronin, T. (2019). A budget for the size of convective self-aggregation. *Quarterly Journal of the Royal Meteorological Society*, *145*(720), 947–966. https://doi.org/10.1002/qj.3468

Biagioli, G., & Tompkins, A. M. (2023). Measuring convective organization. *Journal of the Atmospheric Sciences*, *80*(12), 2769–2789. https://doi.org/10.1175/JAS-D-23-0103.1

Blossey, P. N., Kuang, Z., & Romps, D. M. (2010). Isotopic composition of water in the tropical tropopause layer in cloud-resolving simulations of an idealized tropical circulation. *Journal of Geophysical Research*, *115*(D24). https://doi.org/10.1029/2010JD014554

Bogenschutz, P. A., Clevenger, T. C., Bradley, A. M., Caldwell, P. M., Beydoun, H., Mahfouz, N., et al. (2025). High performance, high fidelity: A GPU-accelerated doubly-periodic configuration of the Simple Cloud-Resolving E3SM Atmosphere Model version 1 (DP-SCREAMv1). *Journal of Advances in Modeling Earth Systems*, *17*(11), e2025MS005127. https://doi.org/10.1029/2025MS005127

Bony, S., Stevens, B., Coppin, D., Becker, T., Reed, K. A., Voigt, A., & Medeiros, B. (2016). Thermodynamic control of anvil cloud amount. *Proceedings of the National Academy of Sciences*, *113*(32), 8927–8932. https://doi.org/10.1073/pnas.1601472113

Bourdin, S., Kluft, L., & Stevens, B. (2021). Dependence of climate sensitivity on the given distribution of relative humidity. *Geophysical Research Letters*, *48*(8), e2021GL092462. https://doi.org/10.1029/2021GL092462

Bretherton, C. S., Blossey, P. N., & Peters, M. E. (2006). Interpretation of simple and cloud-resolving simulations of moist convection–radiation interaction with a mock-walker circulation. *Theoretical and Computational Fluid Dynamics*, *20*(5), 421–442. https://doi.org/10.1007/s00162-006-0029-7

Bretherton, C. S., & Sobel, A. H. (2002). A simple model of a convectively coupled Walker circulation using the weak temperature gradient approximation. *Journal of Climate*, *15*(20), 2907–2920. https://doi.org/10.1175/1520-0442(2002)015<2907:asmoac>2.0.co;2

Ceppi, P., & Gregory, J. M. (2017). Relationship of tropospheric stability to climate sensitivity and Earth's observed radiation budget. *Proceedings of the National Academy of Sciences*, *114*(50), 13126–13131. https://doi.org/10.1073/pnas.1714308114

Charney, J. G. (1963). A note on large-scale motions in the tropics. *Journal of the Atmospheric Sciences*, *20*(6), 607–609. https://doi.org/10.1175/1520-0469(1963)020<0607:anolsm>2.0.co;2

Computational and Information Systems Laboratory. (2023). *Derecho: HPE Cray EX System (University Community Computing)*. NSF National Center for Atmospheric Research. https://doi.org/10.5065/qx9a-pg09

Coppin, D., & Roehrig, R. (2022). Convection self-aggregation in CNRM-CM6-1: Equilibrium and transition sensitivity to surface temperature. *Journal of Advances in Modeling Earth Systems*, *14*(12), e2022MS003064. https://doi.org/10.1029/2022MS003064

Dagan, G., van den Heever, S. C., Stier, P., Abbott, T. H., Barthlott, C., Chaboureau, J.-P., et al. (2025). RCEMIP-ACI: Aerosol-cloud interactions in a multimodel ensemble of radiative-convective equilibrium simulations. *Journal of Advances in Modeling Earth Systems*, *17*(11), e2025MS005141. https://doi.org/10.1029/2025MS005141

Dagan, G., Yeheskel, N., & Williams, A. I. L. (2023). Radiative forcing from aerosol–cloud interactions enhanced by large-scale circulation adjustments. *Nature Geoscience*, *16*(12), 1092–1098. https://doi.org/10.1038/s41561-023-01319-8

Dong, Y., Proistosescu, C., Armour, K. C., & Battisti, D. S. (2019). Attributing historical and future evolution of radiative feedbacks to regional warming patterns using a Green's function approach: The preeminence of the western Pacific. *Journal of Climate*, *32*(17), 5471–5491. https://doi.org/10.1175/JCLI-D-18-0843.1

Emanuel, K. A., David Neelin, J., & Bretherton, C. S. (1994). On large-scale circulations in convecting atmospheres. *Quarterly Journal of the Royal Meteorological Society*, *120*(519), 1111–1143. https://doi.org/10.1002/qj.49712051902

Fu, Q. (1996). An accurate parameterization of the solar radiative properties of cirrus clouds for climate models. *Journal of Climate*, *9*(9), 2058–2082. https://doi.org/10.1175/1520-0442(1996)009⟨2058:AAPOTS⟩2.0.CO;2

Fueglistaler, S., Radley, C., & Held, I. M. (2015). The distribution of precipitation and the spread in tropical upper tropospheric temperature trends in CMIP5/AMIP simulations. *Geophysical Research Letters*, *42*(14), 6000–6007. https://doi.org/10.1002/2015GL064966

Fueglistaler, S., & Silvers, L. (2021). The peculiar trajectory of global warming. *Journal of Geophysical Research: Atmospheres*, *126*(4), e2020JD033629. https://doi.org/10.1029/2020JD033629

Gates, W. L. (1992). An AMS continuing series: Global change–AMIP: The atmospheric model intercomparison project. *Bulletin of the American Meteorological Society*, *73*(12), 1962–1970.

Grabowski, W. W., Yano, J.-I., & Moncrieff, M. W. (2000). Cloud resolving modeling of tropical circulations driven by large-scale SST gradients. *Journal of the Atmospheric Sciences*, *57*(13), 2022–2040. https://doi.org/10.1175/1520-0469(2000)057<2022:crmotc>2.0.co;2

Hartmann, D. L., & Larson, K. (2002). An important constraint on tropical cloud—Climate feedback. *Geophysical Research Letters*, *29*(20), 12-1–12-4. https://doi.org/10.1029/2002GL015835

Held, I. M. (2005). The gap between simulation and understanding in climate modeling. *Bulletin of the American Meteorological Society*, *86*(11), 1609–1614. https://doi.org/10.1175/BAMS-86-11-1609

Held, I. M., Hemler, R. S., & Ramaswamy, V. (1993). Radiative-convective equilibrium with explicit two-dimensional moist convection. *Journal of the Atmospheric Sciences*, *50*(23), 3909–3927. https://doi.org/10.1175/1520-0469(1993)050<3909:rcewet>2.0.co;2

Jeevanjee, N., Hassanzadeh, P., Hill, S., & Sheshadri, A. (2017). A perspective on climate model hierarchies. *Journal of Advances in Modeling Earth Systems*, *9*(4), 1760–1771. https://doi.org/10.1002/2017MS001038

Jenney, A. M., Randall, D. A., & Branson, M. D. (2020). Understanding the response of tropical ascent to warming using an energy balance framework. *Journal of Advances in Modeling Earth Systems*, *12*(6), e2020MS002056. https://doi.org/10.1029/2020MS002056

Kuang, Z. (2012). Weakly forced mock Walker cells. *Journal of the Atmospheric Sciences*, *69*(9), 2759–2786. https://doi.org/10.1175/JAS-D-11-0307.1

Larson, K., & Hartmann, D. L. (2003). Interactions among cloud, water vapor, radiation, and large-scale circulation in the tropical climate. Part II: Sensitivity to spatial gradients of sea surface temperature. *Journal of Climate*, *16*(10), 1441–1455. https://doi.org/10.1175/1520-0442-16.10.1441

Lindzen, R. S., & Nigam, S. (1987). On the role of sea surface temperature gradients in forcing low-level winds and convergence in the tropics. *Journal of the Atmospheric Sciences*, *44*(17), 2418–2436. https://doi.org/10.1175/1520-0469(1987)044<2418:otross>2.0.co;2

Liu, C., & Moncrieff, M. W. (2008). Explicitly simulated tropical convection over idealized warm pools. *Journal of Geophysical Research*, *113*(D21). https://doi.org/10.1029/2008JD010206

Lutsko, N. J., & Cronin, T. W. (2024). The transition to double-celled circulations in mock-Walker simulations. *Geophysical Research Letters*, *51*(14), e2024GL108945. https://doi.org/10.1029/2024GL108945

Mackie, A., & Byrne, M. P. (2023). Effects of circulation on tropical cloud feedbacks in high-resolution simulations. *Journal of Advances in Modeling Earth Systems*, *15*(5), e2022MS003516. https://doi.org/10.1029/2022MS003516

Manabe, S., & Strickler, R. F. (1964). Thermal equilibrium of the atmosphere with a convective adjustment. *Journal of the Atmospheric Sciences*, *21*(4), 361–385. https://doi.org/10.1175/1520-0469(1964)021<0361:teotaw>2.0.co;2

Mandorli, G., & Stubenrauch, C. J. (2024). Assessment of object-based indices to identify convective organization. *Geoscientific Model Development*, *17*(21), 7795–7813. https://doi.org/10.5194/gmd-17-7795-2024

Muller, C. J., O'Gorman, P. A., & Back, L. E. (2011). Intensification of precipitation extremes with warming in a cloud-resolving model. *Journal of Climate*, *24*(11), 2784–2800. https://doi.org/10.1175/2011JCLI3876.1

O'Donnell, G. L., & Wing, A. A. (2024). Precipitation extremes and their modulation by convective organization in RCEMIP. *Journal of Advances in Modeling Earth Systems*, *16*(11), e2024MS004535. https://doi.org/10.1029/2024MS004535

O'Donnell, G. L., & Wing, A. A. (2026). Characteristics of a multi-model ensemble of mock-Walker simulations: Code and derived data [Software]. *Zenodo*. https://doi.org/10.5281/zenodo.18318091

O'Gorman, P. A., & Schneider, T. (2009). The physical basis for increases in precipitation extremes in simulations of 21st-century climate change. *Proceedings of the National Academy of Sciences*, *106*(35), 14773–14777. https://doi.org/10.1073/pnas.0907610106

Pope, K. N., Holloway, C. E., Jones, T. R., & Stein, T. H. M. (2021). Cloud-radiation interactions and their contributions to convective self-aggregation. *Journal of Advances in Modeling Earth Systems*, *13*(9), e2021MS002535. https://doi.org/10.1029/2021MS002535

Pope, K. N., Holloway, C. E., Jones, T. R., & Stein, T. H. M. (2023). Radiation, clouds, and self-aggregation in RCEMIP simulations. *Journal of Advances in Modeling Earth Systems*, *15*(2), e2022MS003317. https://doi.org/10.1029/2022MS003317

Raymond, D. J. (1994). Convective processes and tropical atmospheric circulations. *Quarterly Journal of the Royal Meteorological Society*, *120*(520), 1431–1455. https://doi.org/10.1002/qj.49712052002

Reed, K. A., Silvers, L. G., Wing, A. A., Hu, I.-K., & Medeiros, B. (2021). Using radiative convective equilibrium to explore clouds and climate in the Community Atmosphere Model. *Journal of Advances in Modeling Earth Systems*, *13*(12), e2021MS002539. https://doi.org/10.1029/2021MS002539

Schneider, T., Kaul, C. M., & Pressel, K. G. (2019). Possible climate transitions from breakup of stratocumulus decks under greenhouse warming. *Nature Geoscience*, *12*(3), 163–167. https://doi.org/10.1038/s41561-019-0310-1

Silvers, L. G., Reed, K. A., & Wing, A. A. (2023). The response of the large-scale tropical circulation to warming. *Journal of Advances in Modeling Earth Systems*, *15*(3), e2021MS002966. https://doi.org/10.1029/2021MS002966

Slingo, A. (1989). A GCM parameterization for the shortwave radiative properties of water clouds. *Journal of the Atmospheric Sciences*, *46*(10), 1419–1427. https://doi.org/10.1175/1520-0469(1989)046⟨1419:AGPFTS⟩2.0.CO;2

Sobel, A. H., & Bretherton, C. S. (2000). Modeling tropical precipitation in a single column. *Journal of Climate*, *13*(24), 4378–4392. https://doi.org/10.1175/1520-0442(2000)013⟨4378:MTPIAS⟩2.0.CO;2

Sokol, A. B., & Hartmann, D. L. (2022). Congestus mode invigoration by convective aggregation in simulations of radiative-convective equilibrium. *Journal of Advances in Modeling Earth Systems*, *14*(7), e2022MS003045. https://doi.org/10.1029/2022MS003045

Sokol, A. B., Munteanu, V. A., Blossey, P. N., & Hartmann, D. L. (2025). Internal ocean-atmosphere variability in kilometer-scale radiative-convective equilibrium. *Journal of Advances in Modeling Earth Systems*, *17*(6), e2024MS004567. https://doi.org/10.1029/2024MS004567

Sokol, A. B., Wall, C. J., & Hartmann, D. L. (2024). Greater climate sensitivity implied by anvil cloud thinning. *Nature Geoscience*, *17*(5), 398–403. https://doi.org/10.1038/s41561-024-01420-6

Stauffer, C. L., & Wing, A. A. (2022). Properties, changes, and controls of deep-convecting clouds in radiative-convective equilibrium. *Journal of Advances in Modeling Earth Systems*, *14*(6), e2021MS002917. https://doi.org/10.1029/2021MS002917

Stauffer, C. L., & Wing, A. A. (2023). Explicitly resolved cloud feedbacks in the radiative-convective equilibrium model intercomparison project. *Journal of Advances in Modeling Earth Systems*, *15*(11), e2023MS003738. https://doi.org/10.1029/2023MS003738

Stauffer, C. L., & Wing, A. A. (2024). How does organized convection impact explicitly resolved cloud feedbacks in the Radiative-Convective Equilibrium Model Intercomparison Project? *Journal of Advances in Modeling Earth Systems*, *16*(10), e2023MS003924. https://doi.org/10.1029/2023MS003924

Stephens, G. L., van den Heever, S., & Pakula, L. (2008). Radiative-convective feedbacks in idealized states of radiative-convective equilibrium. *Journal of the Atmospheric Sciences*, *65*(12), 3899–3916. https://doi.org/10.1175/2008JAS2524.1

Tompkins, A. M. (2001). On the relationship between tropical convection and sea surface temperature. *Journal of Climate*, *14*(5), 633–637. https://doi.org/10.1175/1520-0442(2001)014<0633:otrbtc>2.0.co;2

Tompkins, A. M., & Semie, A. G. (2017). Organization of tropical convection in low vertical wind shears: Role of updraft entrainment. *Journal of Advances in Modeling Earth Systems*, *9*(2), 1046–1068. https://doi.org/10.1002/2016MS000802

Williams, A. I. L., & Jeevanjee, N. (2025). Sea-Surface temperature patterns, radiative cooling, and hydrological sensitivity. *Geophysical Research Letters*, *52*(23), e2025GL117734. https://doi.org/10.1029/2025GL117734

Wing, A. A., O'Donnell, G. L., Silvers, L. G., Reed, K. A., Bogenschutz, P. A., Chaboureau, J.-P., et al. (2025). Radiative-Convective equilibrium model intercomparison Project phase II (RCEMIP-II) simulation dataset [Dataset]. *WDC Climate*. https://doi.org/10.1029/2020MS002138

Wing, A. A., Reed, K. A., Satoh, M., Stevens, B., Bony, S., & Ohno, T. (2018). Radiative–convective equilibrium model intercomparison project. *Geoscientific Model Development*, *11*(2), 793–813. https://doi.org/10.5194/gmd-11-793-2018

Wing, A. A., Silvers, L. G., & Reed, K. A. (2024). RCEMIP-II: Mock-walker simulations as phase II of the radiative–convective equilibrium model intercomparison project. *Geoscientific Model Development*, *17*(16), 6195–6225. https://doi.org/10.5194/gmd-17-6195-2024

Wing, A. A., & Singh, M. S. (2024). Control of stability and relative humidity in the Radiative-Convective Equilibrium Model Intercomparison Project. *Journal of Advances in Modeling Earth Systems*, *16*(1), e2023MS003914. https://doi.org/10.1029/2023MS003914

Wing, A. A., Stauffer, C. L., Becker, T., Reed, K. A., Ahn, M.-S., Arnold, N. P., et al. (2020a). Clouds and convective self-aggregation in a multimodel ensemble of radiative-convective equilibrium simulations. *Journal of Advances in Modeling Earth Systems*, *12*(9), e2020MS002138. https://doi.org/10.1029/2020MS002138

Wing, A. A., Stauffer, C. L., Becker, T., Reed, K. A., Ahn, M.-S., Arnold, N. P., et al. (2020b). Radiative-Convective Equilibrium Model Intercomparison Project (RCEMIP) simulation dataset [Dataset]. *WDC Climate*. https://doi.org/10.1029/2020MS002138

Wofsy, J., & Kuang, Z. (2012). Cloud-resolving model simulations and a simple model of an idealized Walker cell. *Journal of Climate*, *25*(23), 8090–8107. https://doi.org/10.1175/JCLI-D-11-00692.1

Yano, J.-I., Grabowski, W. W., & Moncrieff, M. W. (2002). Mean-State convective circulations over large-scale tropical SST gradients. *Journal of the Atmospheric Sciences*, *59*(9), 1578–1592. https://doi.org/10.1175/1520-0469(2002)059⟨1578:MSCCOL⟩2.0.CO;2

Zhang, S., Stier, P., Dagan, G., Zhou, C., & Wang, M. (2023). Sea surface warming patterns drive hydrological sensitivity uncertainties. *Nature Climate Change*, *13*(6), 545–553. https://doi.org/10.1038/s41558-023-01678-5

Zhou, C., Zelinka, M. D., & Klein, S. A. (2016). Impact of decadal cloud variations on the Earth's energy budget. *Nature Geoscience*, *9*(12), 871–874. https://doi.org/10.1038/ngeo2828

References From the Supporting Information

Beljaars, A. C. M., & Holtslag, A. a. M. (1991). Flux parameterization over land surfaces for atmospheric models. *Journal of Applied Meteorology and Climatology*, *30*(3), 327–341. https://doi.org/10.1175/1520-0450(1991)030⟨0327:FPOLSF⟩2.0.CO;2

Bogenschutz, P. A., Eldred, C., & Caldwell, P. M. (2023). Horizontal resolution sensitivity of the simple convection-permitting E3SM atmosphere model in a doubly-periodic configuration. *Journal of Advances in Modeling Earth Systems*, *15*(7), e2022MS003466. https://doi.org/10.1029/2022MS003466

Bogenschutz, P. A., Gettelman, A., Morrison, H., Larson, V. E., Craig, C., & Schanen, D. P. (2013). Higher-order turbulence closure and its impact on climate simulations in the Community Atmosphere Model. *Journal of Climate*, *26*(23), 9655–9676. https://doi.org/10.1175/JCLI-D-13-00075.1

Bogenschutz, P. A., & Krueger, S. K. (2013). A simplified PDF parameterization of subgrid-scale clouds and turbulence for cloud-resolving models. *Journal of Advances in Modeling Earth Systems*, *5*(2), 195–211. https://doi.org/10.1002/jame.20018

Bougeault, P., & Lacarrere, P. (1989). Parameterization of orography-induced turbulence in a mesobeta–scale model. *Monthly Weather Review*, *117*(8), 1872–1890. https://doi.org/10.1175/1520-0493(1989)117⟨1872:POOITI⟩2.0.CO;2

Brown, A. R., Beare, R. J., Edwards, J. M., Lock, A. P., Keogh, S. J., Milton, S. F., & Walters, D. N. (2008). Upgrades to the boundary-layer scheme in the Met Office Numerical Weather Prediction Model. *Boundary-Layer Meteorology*, *128*(1), 117–132. https://doi.org/10.1007/s10546-008-9275-0

Caldwell, P. M., Terai, C. R., Hillman, B., Keen, N. D., Bogenschutz, P., Lin, W., et al. (2021). Convection-permitting simulations with the E3SM global atmosphere model. *Journal of Advances in Modeling Earth Systems*, *13*(11), e2021MS002544. https://doi.org/10.1029/2021MS002544

Chaboureau, J.-P., & Bechtold, P. (2005). Statistical representation of clouds in a regional model and the impact on the diurnal cycle of convection during Tropical Convection, Cirrus and Nitrogen Oxides (TROCCINOX). *Journal of Geophysical Research*, *110*(D17). https://doi.org/10.1029/2004JD005645

Chikira, M., & Sugiyama, M. (2010). A cumulus parameterization with state-dependent entrainment rate. Part I: Description and sensitivity to temperature and humidity profiles. *Journal of the Atmospheric Sciences*, *67*(7), 2171–2193. https://doi.org/10.1175/2010JAS3316.1

Cotton, W. R., Pielke, R. A., Sr., Walko, R. L., Liston, G. E., Tremback, C. J., Jiang, H., et al. (2003). RAMS 2001: Current status and future directions. *Meteorology and Atmospheric Physics*, *82*(1), 5–29. https://doi.org/10.1007/s00703-001-0584-9

Cuxart, J., Bougeault, P., & Redelsperger, J.-L. (2000). A turbulence scheme allowing for mesoscale and large-eddy simulations. *Quarterly Journal of the Royal Meteorological Society*, *126*(562), 1–30. https://doi.org/10.1002/qj.49712656202

Danabasoglu, G., Lamarque, J.-F., Bacmeister, J., Bailey, D. A., DuVivier, A. K., Edwards, J., et al. (2020). The Community Earth System Model version 2 (CESM2). *Journal of Advances in Modeling Earth Systems*, *12*(2), e2019MS001916. https://doi.org/10.1029/2019MS001916

Edwards, J. M., & Slingo, A. (1996). Studies with a flexible new radiation code. I: Choosing a configuration for a large-scale model. *Quarterly Journal of the Royal Meteorological Society*, *122*(531), 689–719. https://doi.org/10.1002/qj.49712253107

Fouquart, Y., & Bonnel, B. (1980). Computations of solar heating of the Earth's atmosphere: A new parameterization. *Contributions to Atmospheric Physics*, *53*(1), 35–62.

Gasparini, B., Atlas, R., Voigt, A., Krämer, M., & Blossey, P. N. (2025). Tropical cirrus evolution in a kilometer-scale model with improved ice microphysics. *Atmospheric Chemistry and Physics*, *25*(17), 9957–9979. https://doi.org/10.5194/acp-25-9957-2025

Gettelman, A., & Morrison, H. (2015). Advanced two-moment bulk microphysics for global models. Part I: Off-line tests and comparison with other schemes. *Journal of Climate*, *28*(3), 1268–1287. https://doi.org/10.1175/JCLI-D-14-00102.1

Gettelman, A., Morrison, H., Santos, S., Bogenschutz, P., & Caldwell, P. M. (2015). Advanced two-moment bulk microphysics for global models. Part II: Global model solutions and aerosol–cloud interactions. *Journal of Climate*, *28*(3), 1288–1307. https://doi.org/10.1175/JCLI-D-14-00103.1

Golaz, J.-C., Larson, V. E., & Cotton, W. R. (2002). A PDF-based model for boundary layer clouds. Part I: Method and model description. *Journal of the Atmospheric Sciences*, *59*(24), 3540–3551. https://doi.org/10.1175/1520-0469(2002)059⟨3540:APBMFB⟩2.0.CO;2

Golaz, J.-C., Van Roekel, L. P., Zheng, X., Roberts, A. F., Wolfe, J. D., Lin, W., et al. (2022). The DOE E3SM model version 2: Overview of the physical model and initial model evaluation. *Journal of Advances in Modeling Earth Systems*, *14*(12), e2022MS003156. https://doi.org/10.1029/2022MS003156

Gregory, D., & Rowntree, P. R. (1990). A mass flux convection scheme with representation of cloud ensemble characteristics and stability-dependent closure. *Monthly Weather Review*, *118*(7), 1483–1506. https://doi.org/10.1175/1520-0493(1990)118⟨1483:AMFCSW⟩2.0.CO;2

Guérémy, J. F. (2011). A continuous buoyancy based convection scheme: One- and three-dimensional validation. *Tellus Series A-dynamic Meteorology and Oceanography*, *63*(4), 687–706. https://doi.org/10.1111/j.1600-0870.2011.00521.x

Hannah, W., & Pressel, K. (2022). A method for transporting cloud-resolving model variance in a multiscale modeling framework. *Geoscientific Model Development*, *15*(24), 8999–9013. https://doi.org/10.5194/gmd-15-8999-2022

Hill, G. E. (1974). Factors controlling the size and spacing of cumulus clouds as revealed by numerical experiments. *Journal of the Atmospheric Sciences*, *31*(3), 646–673. https://doi.org/10.1175/1520-0469(1974)031<0646:fctsas>2.0.co;2

Hohenegger, C., Korn, P., Linardakis, L., Redler, R., Schnur, R., Adamidis, P., et al. (2023). ICON-Sapphire: Simulating the components of the Earth system and their interactions at kilometer and subkilometer scales. *Geoscientific Model Development*, *16*(2), 779–811. https://doi.org/10.5194/gmd-16-779-2023

Holtslag, A. A. M., & Boville, B. A. (1993). Local versus nonlocal boundary-layer diffusion in a global climate model. *Journal of Climate*, *6*(10), 1825–1842. https://doi.org/10.1175/1520-0442(1993)006⟨1825:LVNBLD⟩2.0.CO;2

Iacono, M. J., Delamere, J. S., Mlawer, E. J., Shephard, M. W., Clough, S. A., & Collins, W. D. (2008). Radiative forcing by long-lived greenhouse gases: Calculations with the AER radiative transfer models. *Journal of Geophysical Research*, *113*(D13). https://doi.org/10.1029/2008JD009944

Jung, J.-H., & Arakawa, A. (2008). A three-dimensional anelastic model based on the vorticity equation. *Monthly Weather Review*, *136*(1), 276–294. https://doi.org/10.1175/2007MWR2095.1

Khairoutdinov, M. F., & Randall, D. A. (2003). Cloud resolving modeling of the ARM summer 1997 IOP: Model formulation, results, uncertainties, and sensitivities. *Journal of the Atmospheric Sciences*, *60*(4), 607–625. https://doi.org/10.1175/1520-0469(2003)060⟨0607:CRMOTA⟩2.0.CO;2

Krueger, S. K., Fu, Q., Liou, K. N., & Chin, H.-N. S. (1995). Improvements of an ice-phase microphysics parameterization for use in numerical simulations of tropical convection. *Journal of Applied Meteorology and Climatology*, *34*(1), 281–287. https://doi.org/10.1175/1520-0450-34.1.281

Lac, C., Chaboureau, J.-P., Masson, V., Pinty, J.-P., Tulet, P., Escobar, J., et al. (2018). Overview of the Meso-NH model version 5.4 and its applications. *Geoscientific Model Development*, *11*(5), 1929–1969. https://doi.org/10.5194/gmd-11-1929-2018

Larson, V. E., & Golaz, J.-C. (2005). Using probability density functions to derive consistent closure relationships among higher-order moments. *Monthly Weather Review*, *133*(4), 1023–1042. https://doi.org/10.1175/MWR2902.1

Larson, V. E., Golaz, J.-C., & Cotton, W. R. (2002). Small-scale and mesoscale variability in cloudy boundary layers: Joint probability density functions. *Journal of the Atmospheric Sciences*, *59*(24), 3519–3539. https://doi.org/10.1175/1520-0469(2002)059⟨3519:SSAMVI⟩2.0.CO;2

Lilly, D. K. (1962). On the numerical simulation of buoyant convection. *Tellus*, *14*(2), 148–172. https://doi.org/10.1111/j.2153-3490.1962.tb00128.x

Lilly, D. K. (1967). The representation of small-scale turbulence in numerical simulation experiments. In *Proceedings of IBM scientific computing Symposium on environmental sciences* (pp. 195–210). IBM.

Lin, Y.-L., Farley, R. D., & Orville, H. D. (1983). Bulk parameterization of the snow field in a cloud model. *Journal of Applied Meteorology and Climatology*, *22*(6), 1065–1092. https://doi.org/10.1175/1520-0450(1983)022⟨1065:BPOTSF⟩2.0.CO;2

Lock, A. P. (2001). The numerical representation of entrainment in parameterizations of boundary layer turbulent mixing. *Monthly Weather Review*, *129*(5), 1148–1163. https://doi.org/10.1175/1520-0493(2001)129⟨1148:TNROEI⟩2.0.CO;2

Lock, A. P., Brown, A. R., Bush, M. R., Martin, G. M., & Smith, R. N. B. (2000). A new boundary layer mixing scheme. Part I: Scheme description and single-column model tests. *Monthly Weather Review*, *128*(9), 3187–3199. https://doi.org/10.1175/1520-0493(2000)128⟨3187:ANBLMS⟩2.0.CO;2

Lopez, P. (2002). Implementation and validation of a new prognostic large-scale cloud and precipitation scheme for climate and data-assimilation purposes. *Quarterly Journal of the Royal Meteorological Society*, *128*(579), 229–257. https://doi.org/10.1256/00359000260498879

Lord, S. J., Willoughby, H. E., & Piotrowicz, J. M. (1984). Role of a parameterized ice-phase microphysics in an axisymmetric, nonhydrostatic tropical cyclone model. *Journal of the Atmospheric Sciences*, *41*(19), 2836–2848. https://doi.org/10.1175/1520-0469(1984)041⟨2836:ROAPIP⟩2.0.CO;2

Manners, J., Edwards, J. M., Hill, P., & Thelen, J.-C. (2015). *SOCRATES (suite of community radiative transfer codes based on edwards and slingo) technical guide*. Office.

Mlawer, E. J., Taubman, S. J., Brown, P. D., Iacono, M. J., & Clough, S. A. (1997). Radiative transfer for inhomogeneous atmospheres: RRTM, a validated correlated-k model for the longwave. *Journal of Geophysical Research*, *102*(D14), 16663–16682. https://doi.org/10.1029/97JD00237

Moon, I.-J., Ginis, I., Hara, T., & Thomas, B. (2007). A physics-based parameterization of air–sea momentum flux at high wind speeds and its impact on hurricane intensity predictions. *Monthly Weather Review*, *135*(8), 2869–2878. https://doi.org/10.1175/MWR3432.1

Morcrette, J.-J., Barker, H. W., Cole, J. N. S., Iacono, M. J., & Pincus, R. (2008). Impact of a new radiation package, McRad, in the ECMWF Integrated Forecasting System. *Monthly Weather Review*, *136*(12), 4773–4798. https://doi.org/10.1175/2008MWR2363.1

Morrison, H., Curry, J. A., & Khvorostyanov, V. I. (2005). A new double-moment microphysics parameterization for application in cloud and climate models. Part I: Description. *Journal of the Atmospheric Sciences*, *62*(6), 1665–1677. https://doi.org/10.1175/JAS3446.1

Morrison, H., & Milbrandt, J. A. (2015). Parameterization of cloud microphysics based on the prediction of bulk ice particle properties. Part I: Scheme description and idealized tests. *Journal of the Atmospheric Sciences*, *72*(1), 287–311. https://doi.org/10.1175/JAS-D-14-0065.1

Nakanishi, M. (2001). Improvement of the Mellor–Yamada turbulence closure model based on large-eddy simulation data. *Boundary-Layer Meteorology*, *99*(3), 349–378. https://doi.org/10.1023/A:1018915827400

Nakanishi, M., & Niino, H. (2004). An improved Mellor–Yamada level-3 model with condensation physics: Its design and verification. *Boundary-Layer Meteorology*, *112*(1), 1–31. https://doi.org/10.1023/B:BOUN.0000020164.04146.98

Nishizawa, S., Yashiro, H., Sato, Y., Miyamoto, Y., & Tomita, H. (2015). Influence of grid aspect ratio on planetary boundary layer turbulence in large-eddy simulations. *Geoscientific Model Development*, *8*(10), 3393–3419. https://doi.org/10.5194/gmd-8-3393-2015

Park, S., & Bretherton, C. S. (2009). The University of Washington shallow convection and moist turbulence schemes and their impact on climate simulations with the community atmosphere model. *Journal of Climate*, *22*(12), 3449–3469. https://doi.org/10.1175/2008JCLI2557.1

Pergaud, J., Masson, V., Malardel, S., & Couvreux, F. (2009). A parameterization of dry thermals and shallow cumuli for mesoscale numerical weather prediction. *Boundary-Layer Meteorology*, *132*(1), 83–106. https://doi.org/10.1007/s10546-009-9388-0

Pincus, R., Mlawer, E. J., & Delamere, J. S. (2019). Balancing accuracy, efficiency, and flexibility in radiation calculations for dynamical models. *Journal of Advances in Modeling Earth Systems*, *11*(10), 3074–3089. https://doi.org/10.1029/2019MS001621

Pinty, J., & Jabouille, P. (1998). A mixed-phase cloud parameterization for use in mesoscale non-hydrostatic model: Simulations of a squall line and of orographic precipitations. In *Preprints* (pp. 217–220). American Meteorological Society.

Piriou, J.-M., Redelsperger, J.-L., Geleyn, J.-F., Lafore, J.-P., & Guichard, F. (2007). An approach for convective parameterization with memory: Separating microphysics and transport in grid-scale equations. *Journal of the Atmospheric Sciences*, *64*(11), 4127–4139. https://doi.org/10.1175/2007JAS2144.1

Roehrig, R., Beau, I., Saint-Martin, D., Alias, A., Decharme, B., Guérémy, J.-F., et al. (2020). The CNRM global atmosphere model ARPEGE-Climat 6.3: Description and evaluation. *Journal of Advances in Modeling Earth Systems*, *12*(7), e2020MS002075. https://doi.org/10.1029/2020MS002075

Romps, D. M. (2008). The dry-entropy budget of a moist atmosphere. *Journal of the Atmospheric Sciences*, *65*(12), 3779–3799. https://doi.org/10.1175/2008JAS2679.1

Saleeby, S. M., & Cotton, W. R. (2008). A binned approach to cloud-droplet riming implemented in a bulk microphysics model. *Journal of Applied Meteorology and Climatology*, *47*(2), 694–703. https://doi.org/10.1175/2007JAMC1664.1

Saleeby, S. M., & van den Heever, S. C. (2013). Developments in the CSU-RAMS aerosol model: Emissions, nucleation, regeneration, deposition, and radiation. *Journal of Applied Meteorology and Climatology*, *52*(12), 2601–2622. https://doi.org/10.1175/JAMC-D-12-0312.1

Sato, Y., Nishizawa, S., Yashiro, H., Miyamoto, Y., Kajikawa, Y., & Tomita, H. (2015). Impacts of cloud microphysics on trade wind cumulus: Which cloud microphysics processes contribute to the diversity in a large eddy simulation? *Progress in Earth and Planetary Science*, *2*(1), 23. https://doi.org/10.1186/s40645-015-0053-6

Sekiguchi, M., & Nakajima, T. (2008). A k-distribution-based radiation code and its computational optimization for an atmospheric general circulation model. *Journal of Quantitative Spectroscopy and Radiative Transfer*, *109*(17), 2779–2793. https://doi.org/10.1016/j.jqsrt.2008.07.013

Shutts, G. J., & Gray, M. E. B. (1994). A numerical modelling study of the geostrophic adjustment process following deep convection. *Quarterly Journal of the Royal Meteorological Society*, *120*(519), 1145–1178. https://doi.org/10.1002/qj.49712051903

Smagorinsky, J. (1963). General circulation experiments with the primitive equations. *Monthly Weather Review*, *91*(3), 99–164. https://doi.org/10.1175/1520-0493(1963)091⟨0099:GCEWTP⟩2.3.CO;2

Smith, R. N. B. (1990). A scheme for predicting layer clouds and their water content in a general circulation model. *Quarterly Journal of the Royal Meteorological Society*, *116*(492), 435–460. https://doi.org/10.1002/qj.49711649210

Stratton, R. A., Senior, C. A., Vosper, S. B., Folwell, S. S., Boutle, I. A., Earnshaw, P. D., et al. (2018). A Pan-African convection-permitting regional climate simulation with the Met Office Unified Model: CP4-Africa. *Journal of Climate*, *31*(9), 3485–3508. https://doi.org/10.1175/JCLI-D-17-0503.1

Tatebe, H., Ogura, T., Nitta, T., Komuro, Y., Ogochi, K., Takemura, T., et al. (2019). Description and basic evaluation of simulated mean state, internal variability, and climate sensitivity in MIROC6. *Geoscientific Model Development*, *12*(7), 2727–2765. https://doi.org/10.5194/gmd-12-2727-2019

Taylor, M. A., Guba, O., Steyer, A., Ullrich, P. A., Hall, D. M., & Eldred, C. (2020). An energy consistent discretization of the nonhydrostatic equations in primitive variables. *Journal of Advances in Modeling Earth Systems*, *12*(1), e2019MS001783. https://doi.org/10.1029/2019MS001783

Tomita, H. (2008). New microphysical schemes with five and six categories by diagnostic generation of cloud ice. *Journal of the Meteorological Society of Japan. Series II*, *86A*, 121–142. https://doi.org/10.2151/jmsj.86A.121

Voldoire, A., Saint-Martin, D., Sénési, S., Decharme, B., Alias, A., Chevallier, M., et al. (2019). Evaluation of CMIP6 DECK experiments with CNRM-CM6-1. *Journal of Advances in Modeling Earth Systems*, *11*(7), 2177–2213. https://doi.org/10.1029/2019MS001683

Walters, D., Baran, A. J., Boutle, I., Brooks, M., Earnshaw, P., Edwards, J., et al. (2019). The met office unified model global atmosphere 7.0/7.1 and JULES global land 7.0 configurations. *Geoscientific Model Development*, *12*(5), 1909–1963. https://doi.org/10.5194/gmd-12-1909-2019

Wilson, D. K. (2001). An alternative function for the wind and temperature gradients in unstable surface layers. *Boundary-Layer Meteorology*, *99*(1), 151–158. https://doi.org/10.1023/A:1018718707419

Wilson, D. R., & Ballard, S. P. (1999). A microphysically based precipitation scheme for the UK meteorological office unified model. *Quarterly Journal of the Royal Meteorological Society*, *125*(557), 1607–1636. https://doi.org/10.1002/qj.49712555707

Wood, N., Staniforth, A., White, A., Allen, T., Diamantakis, M., Gross, M., et al. (2014). An inherently mass-conserving semi-implicit semi-Lagrangian discretization of the deep-atmosphere global non-hydrostatic equations. *Quarterly Journal of the Royal Meteorological Society*, *140*(682), 1505–1520. https://doi.org/10.1002/qj.2235

Wu, C.-M., & Arakawa, A. (2011). Inclusion of surface topography into the Vector Vorticity Equation Model (VVM). *Journal of Advances in Modeling Earth Systems*, *3*(2). https://doi.org/10.1029/2011MS000061

Wu, C.-M., Lin, H.-C., Cheng, F.-Y., & Chien, M.-H. (2019). Implementation of the land surface processes into a Vector Vorticity Equation Model (VVM) to study its impact on afternoon thunderstorms over complex topography in Taiwan. *Asia-Pacific Journal of Atmospheric Sciences*, *55*(4), 701–717. https://doi.org/10.1007/s13143-019-00116-x

Yamaguchi, T., Randall, D. A., & Khairoutdinov, M. F. (2011). Cloud modeling tests of the ULTIMATE–MACHO scalar advection scheme. *Monthly Weather Review*, *139*(10), 3248–3264. https://doi.org/10.1175/MWR-D-10-05044.1

Yang, Q., Hannah, W. M., & Leung, L. R. (2022). Convective momentum transport and its impact on the Madden-Julian Oscillation in E3SM-MMF. *Journal of Advances in Modeling Earth Systems*, *14*(11), e2022MS003206. https://doi.org/10.1029/2022MS003206

Zhang, G., & McFarlane, N. A. (1995). Sensitivity of climate simulations to the parameterization of cumulus convection in the Canadian climate centre general circulation model. *Atmosphere-Ocean*, *33*(3), 407–446. https://doi.org/10.1080/07055900.1995.9649539